# SANDIA REPORT

SAND2004-6322
Unlimited Release
Printed February 2005

# Ultra-Lightweight Telescope with MEMS Adaptive Optic for Distortion Correction

Olga Blum Spahn, Daryl Dagel, William Cowan, Fawn Gass, Grant Grossetete, Bill Sweatt, Alex Grine, Sita Mani, Paul Resnick, David Adams, Michael Shaw

Prepared by
Sandia National Laboratories
Albuquerque, New Mexico 87185 and Livermore, California 94550

Sandia is a multiprogram laboratory operated by Sandia Corporation,
a Lockheed Martin Company, for the United States Department of Energy's
National Nuclear Security Administration under Contract DE-AC04-94AL85000.



Sandia National Laboratories

Issued by Sandia National Laboratories, operated for the United States Department of Energy by Sandia Corporation.



Available to DOE and DOE contractors from
U.S. Department of Energy
Office of Scientific and Technical Information
P.O. Box 62
Oak Ridge, TN 37831

Telephone: (865)576-8401
Facsimile: (865)576-5728
E-Mail: reports@adonis.osti.gov
Online ordering: http://www.osti.gov/bridge

Available to the public from
U.S. Department of Commerce
National Technical Information Service
5285 Port Royal Rd
Springfield, VA 22161

Telephone: (800)553-6847
Facsimile: (703)605-6900
E-Mail: orders@ntis.fedworld.gov
Online order: http://www.ntis.gov/help/ordermethods.asp?loc=7-4-0#online

SAND2004-6322
Unlimited Release
Printed December 2004

# Ultra-Lightweight Telescope with MEMS Adaptive Optic for Distortion Correction

Olga Blum Spahn, Daryl Dagel, William Cowan,
Fawn Gass, Grant Grossetete, Bill Sweatt,
Alex Grine, Sita Mani, Paul Resnick, David Adams, Michael Shaw

Sandia National Laboratories
P. O. Box 5800
Albuquerque, NM 87185-0603



## ABSTRACT

Recent world events have underscored the need for a satellite based persistent global surveillance capability. To be useful, the satellite must be able to continuously monitor objects the size of a person anywhere on the globe and do so at a low cost.

One way to satisfy these requirements involves a constellation of satellites in low earth orbit capable of resolving a spot on the order of 20 cm. To reduce cost of deployment, such a system must be dramatically lighter than a traditional satellite surveillance system with a high spatial resolution. The key to meeting this requirement is a lightweight optics system with a deformable primary and secondary mirrors and an adaptive optic subsystem correction of wavefront distortion. This proposal is concerned with development of MEMS micromirrors for correction of aberrations in the primary mirror and improvement of image quality, thus reducing the optical requirements on the deployable mirrors. To meet this challenge, MEMS micromirrors must meet stringent criteria on their performance in terms of flatness, roughness and resolution of position. Using Sandia's SUMMIT foundry which provides the world's most sophisticated surface MEMS technology as well as novel designs optimized by finite element analysis will meet severe requirements on mirror travel range and accuracy.

**Intentionally left blank**

# Table of Contents

1. Introduction
2. Optical Issues For Surface-Micromachined MEMS Mirrors
3. Mirror Designs
4. Characterization of beams and mirrors
5. Modeling and Simulation Of Mirror Figure
6. Actuators design
7. Arrays
8. Future Work

# 1 Introduction

In general adaptive optics systems are used to correct phase errors in a distorted wavefront from an optical signal. As seen in Fig. 1, adaptive optic systems usually consist of a wave front sensor, focusing optics, including the adaptive mirror or deformable MEMS mirror such as described in this study, a spatial light modulator, which corrects detected wave front phase errors, imaging sensors, and the electronics associated with the control system, which make the system work coherently. These types of systems have the purpose of improving image quality by reducing phase aberrations introduced when the wavefront travels through a turbulent atmosphere or aberrations introduced by the optical system itself [1].

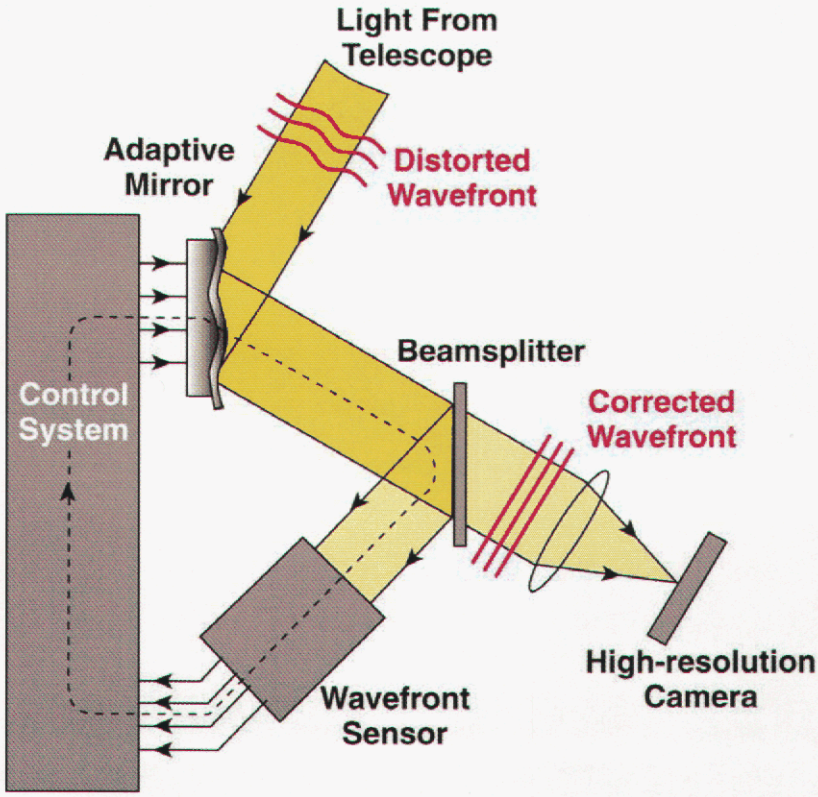


**Figure 1 Adaptive Optics System [2]**

We propose to design, fabricate and test a MEMS micromirror array for a specific adaptive optic system that would enable an ultra lightweight telescope without compromising its optical quality. Ultra lightweight telescope would significantly decrease the weight and thus the cost of a satellite, which in turn would allow a constellation of satellites to be launched for a price of a single, traditional satellite. This can be realized by employing an aberration correcting MEMS micromirror array to improve the optical performance of a lightweight deployable primary mirror. A sample system concept is shown in Figure 2.

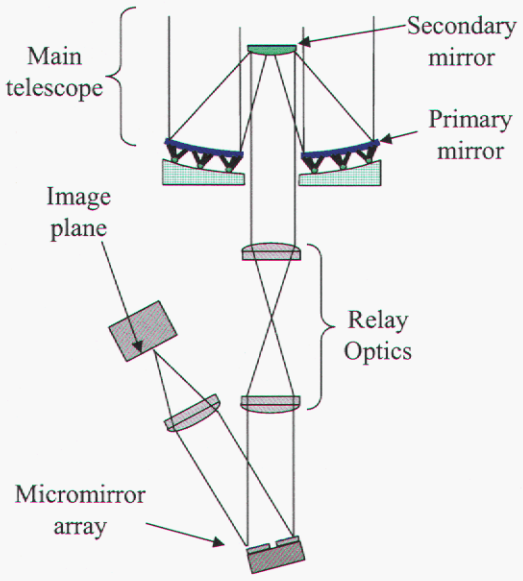


**Figure 2 an example of a telescope system employing aberration correcting MEMS micromirror array**

The desired MEMS micromirror based wavefront correction system will reduce the RMS wavefront error by a factor of about 100. Additional reduction in the RMS error can be obtained with a coarse correction of the primary mirror and would be expected to reduce the aberrations from roughly 50 λ RMS down to about 5 λ RMS. Further reduction from 5 λ to 0.05 λ (diffraction-limited) would be accomplished by the fine corrector comprised of the MEMS micromirror array. Assuming a 1 m section of the primary/secondary, a 40 mm micromirror array can be expected.

To fulfill their role in correcting aberrations of the lightweight primary mirror MEMS micromirror arrays must meet stringent performance criteria. Preliminary calculations indicate trade-offs between mirror size and functionality. Thus an array of fewer (~20x20) and larger (~2mm) micromirrors capable of tip/tilt and piston motion can provide the same level of aberration correction (~100x) as an array of more (~60x60) and (~700 μm) piston only micromirrors. There are advantages and disadvantages to both scenarios. While fewer, larger mirrors simplify the necessary electrical wiring they must maintain the same stringent requirement on flatness as the smaller mirrors. Furthermore, more complex mirror designs are necessary to produce both tip/tilt as well as piston motion. Additionally, the mirror array must be individually addressable, possess a high fill factor and be highly reflective. For the purposes of this program, we will focus on an as large an array as can be interconnected with surface traces. The problem of interconnecting a large number of elements is an important one and is being addressed under the auspices of another LDRD program, but is beyond the scope of this activity.

Assuming incident radiation in the visible regime and requiring a diffraction limited image (aberrations <λ/20 using Strehl ratio of 90%), implies rigorous performance characteristics in terms of flatness, curvature and travel range and resolution for the individual mirrors. Correcting the wavefront error by a factor of 100 requires that the mirror be able to travel from a distance equivalent to 5λ. It is desirable to travel this distance with 8-bit accuracy. Furthermore, mirrors should be flat to within λ/20 after the reflective coating is applied.

Depending on the desired type of mirror and interconnect complexity, mirror size can vary from 1-2 mm size to 100 μm with a corresponding increase in the number of mirrors in the array. Required mirror characteristics are summarized in Table I.

Table I required mirror characteristics

| Characteristic | Value |
|---|---|
| Mirror Size | ~1 – 2 mm |
| Mirror Travel Range | ~5λ |
| Travel Resolution | 8 bits |
| Surface Quality | <λ/20 |
| Array Size | From 20x20 to 60x60 |
| Mirror Motion Type | Tip/tilt/piston |

### 1.1 Scope of the program

Although smooth, flat mirrors are routinely fabricated on the macro-scale, mirrors made of surface micro-machined polycrystalline silicon (polysilicon) do not yet have the requisite optical performance demanded by some applications such as adaptive optics. In the past, MEMS design was largely empirical, where many different iterations of the design were created and sent through a foundry process in a relatively short turnaround time. When these processes become more complex, more time is needed and costs increase, so some type of understanding of the device behavior is needed before fabrication. In this project, a predictive modeling capability is developed which relates the relevant structural parameters defined by the design and fabrication process to the mechanical performance and optical properties of micromirrors. The goal is to optimize the optical characteristics of micromirrors through modeling and characterization for a variety of adaptive optic microsystem applications. Another aspect of this project involves development of high stroke actuators capable of high positional resolution. Finally, it is our goal to demonstrate large mirror arrays, which involves mirror and actuator design, fabrication, metallization, packaging and drive board development and realization. Thus the final results of this program will be a MEMS-based adaptive optic system, ready for insertion into an ultra lightweight telescope system or any other optical system in the need of wavefront correction.

# 2 Optical Issues for Surface-Micromachined MEMS Mirrors

Mirrors made of surface micro-machined polysilicon do not yet have the requisite optical performance required by some demanding areas such as in adaptive optics. There are several types of deformation of SUMMiT fabricated MEMS mirrors that contribute to degradation of their optical performance. Starting with the largest spatial scale effect is the array planarity. This refers to vertical registration of mirrors with respect to one another in the array and is mostly governed by effects such as process uniformity and wafer curvature (for very large arrays). Next effect is the individual mirror curvature, which is described in the section 2.1. It can be caused by stress and stress gradients in the polysilicon layers comprising the mirror, stress in the reflective coatings on the mirror surface and temperature variations which cause changes in curvature due to differential stress as a result in different coefficients of thermal expansion in the polysilicon and the reflective top layer. Section 2.2 describes the next deformation due to print through effects and etch release holes. Finally, deformation on the finest spatial scale, due to root mean square roughness of the polysilicon material itself is described in section 2.3.

## 2.1 Curvature: Residual Stress and Stress Gradients

Polysilicon MEMS are commonly deposited by chemical vapor deposition and are therefore susceptible to thin film residual stress and stress gradients. This is exacerbated by the fact that the polysilicon layers comprising the mirrors are quite thin – 2.25 μm for poly4, the top polysilicon layer in SUMMiT. In addition to curvature from thin-film stresses, several other factors must be considered when designing MEMS mirrors, including light scattering and losses due to surface topography. As a result, design features such as low stress polysilicon films, reduced number of etch release holes, non-periodic etch release holes, multi-layers, reinforced mirrors and low-stress reflective films must be incorporated to minimize these contributions to overall system loss. Residual stress is a major factor in designing optically flat mirrors due to the highly curved surfaces that may result if residual stress and stress gradients are not small. There are several possible sources of residual stress including thermal cycling, dopants, impurities, grain growth and grain orientation [3]. Every layer in SUMMiT is annealed after deposition to reduce the amount of residual stress. The polysilicon films possess ~10 MPa of residual stress after annealing, while the sacrificial oxide films possess much more, on the order of 300 MPa.

In order to quantify the amount of stress and stress gradient in the thin-film layers of polysilicon, MEMS test structures are created and evaluated on the wafer of concern. These test structures consist of varying sizes of cantilever, or fixed-free beams, which curl under a stress gradient and fixed-fixed beams which will buckle under residual stress. Figs. 3 and 4 show interferograms of several cantilever (200 μm - 1000 μm long) and fixed-fixed (400 μm and 600 μm long) beam test structures, respectively.

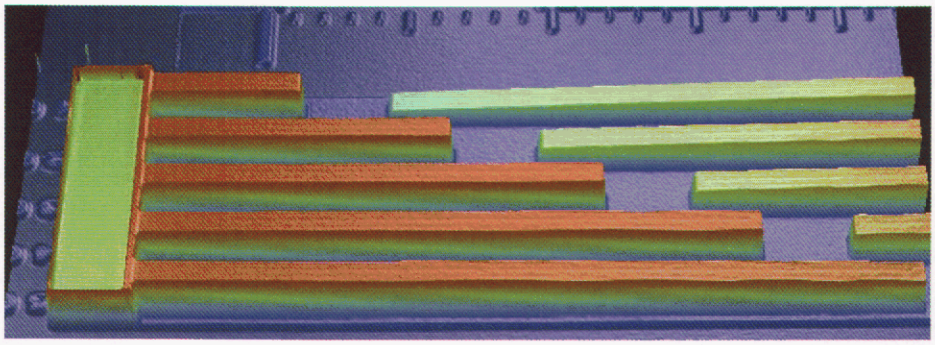

**Figure 3 3-D Interferogram of cantilever beams (200 µm - 1000 µm long).**

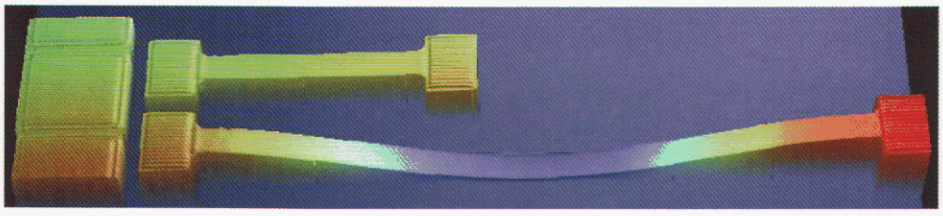

**Figure 4 Fixed-fixed beams: longer beam (600 µm) is buckled.**

In several mirror designs discussed in this study, a "trapping oxide" between polysilicon layers is used. A "trapping oxide" consists of a patterned sacrificial oxide layer directly on the polysilicon layer below followed by a deposited polysilicon on top of the oxide that joins the polysilicon surface below, thus keeping the oxide trapped between the polysilicon layers. One of the results of trapping oxide is the formation of mechanical struts, or vertical stiffening members that create deep topographical features in the top surface (Fig. 5). This adverse effect can be mitigated by using a smaller pattern in the oxide, which is discussed in detail in section 4.

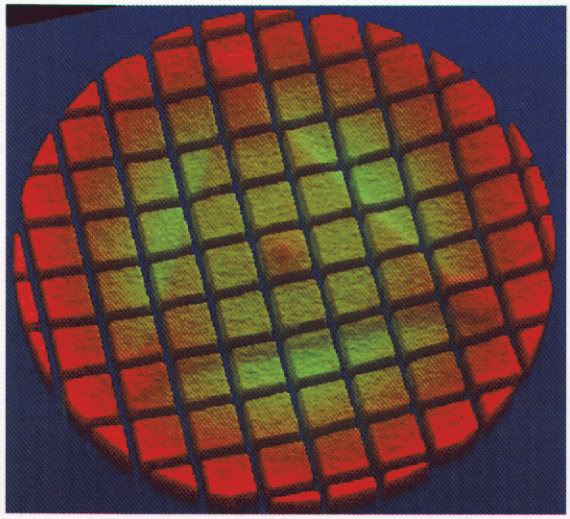

**Figure 5 Interferogram of 500 µm mirror with trapped oxide and vertical stiffening members.**

Due to the high stress in the sacrificial oxide layer, severe curvature in the mirror surface is created. These designs are discussed in detail in section 4. Another variable that greatly affects curvature is the relative thickness of the polysilicon layers that provide the mirror surface. In the SUMMiT process, MMpoly3 and MMpoly4 are nominally the same thickness (2.25 μm). Customizing the thickness of the mirror by including only one of these layers, trapping oxide between them, or laminating them together (MMpoly3 and MMpoly4 joined without an air gap) will dramatically change the curvature profile of the mirror. Surface curvature is the largest factor when considering optical effects in MEMS mirrors. The issues of stress gradients and residual stress will be covered in detail in Sections 5 and 6.

## 2.2 Print-through Effects

Although chemical-mechanical polishing (CMP) on sacrificial oxide layers (sacox3 and sacox4) is a standard part of the SUMMiT V process which serves to remove adverse topographical effects, there still exists a small amount of print-through topography (~10-20 nm) [4] that results from the interaction of the CMP, annealing cycles and pattern density issues associated with the designs. It is called print-through because underlying polysilicon patterns appear in relief on the MMpoly3 and MMpoly4 layers. Unlike the topography generated by oxide cuts in the mirror design, this non-planarity appears regardless of whether oxide is trapped or released. The print-through effect is seen clearly in Fig. 6 in two separate mirrors. Although the image is exaggerated in the z-scale, the underlying triangular structure pattern unmistakably appears on the top surface of the mirror.

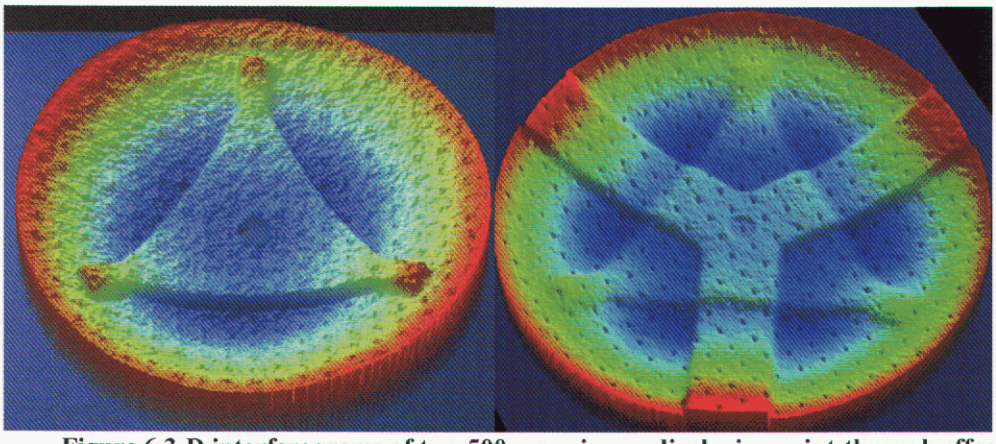

**Figure 6 3-D interferograms of two 500 μm mirrors displaying print-through effects.**

In order for a mechanical polysilicon layer to be released the sacrificial oxide must be removed. The oxide is removed from below polysilicon structures through small (2 μm x 2 μm) etch release holes to provide etch access. These etch release holes, as displayed in Fig. 7, create a hole in the top surface of the mirror. The hole causes some light loss when reflecting off the mirror surface. The reflected light loss can be randomly reflected if the etch release holes are not periodic or the holes have a large pitch. Notice that the holes in Fig. 7 are periodic, and are tightly spaced. Design rules state that etch release holes must be spaced at a certain distance in order for the oxide beneath to be fully removed. This causes problems for eliminating this optical light loss. However, with some clever arrangements of etch release holes, the problem can be reduced.

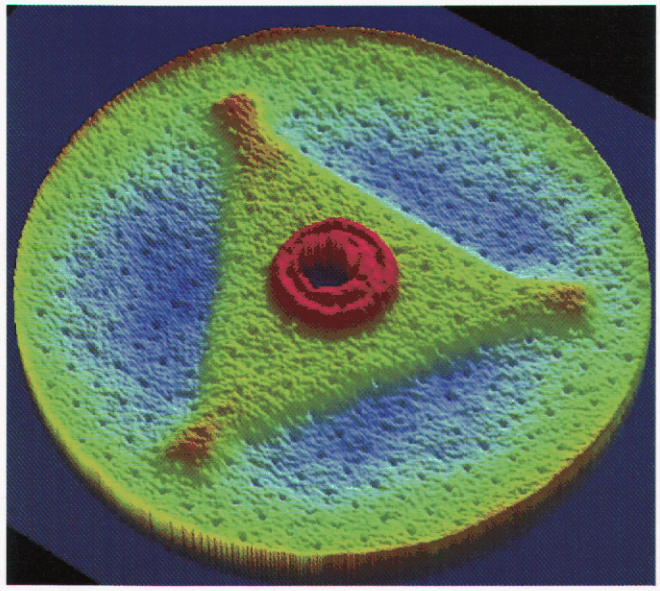

**Figure 7 Interferogram of 500 μm mirror that displays etch release holes (black dots).**

## 2.3 RMS Roughness

Surface roughness is also an important optical issue that needs to be addressed when using surface micromachining. Roughness scatters light and causes a halo to form, acting as a source of loss and stray light in the system. Surface roughness is a direct result of the polycrystalline nature of polysilicon, and while a final polishing of the top surface can further reduce the roughness, it is not a routine step in most surface micromachining processes. Fig. 7 displays a 3-D interferogram of a 500 μm mirror surface where roughness effects are evident on the polysilicon surface.

## 2.4 Summary

Optical issues are very important to consider when using surface micromachining techniques, specifically MEMS structures. These issues are, in order of importance, curvature from stress in the polysilicon layers, print-through effects, RMS roughness, and etch release holes. These optical issues cause astigmatism, a drop in efficiency of the beam, light scattering and loss, respectively. These adverse optical effects are somewhat controllable, depending on the mirror design and process variations.

# 3 Mirror Designs

## 3.1 Background

Micro-mirrors have been fabricated using SUMMiT V™ technology in the past [5-14]. Many of these designs utilize only a single polysilicon layer for the mirror surface and use the remaining layers for actuators and electrical connections. Applications such as high-speed optical switching require a more rigid surface, thus it is common to laminate two polysilicon layers to increase rigidity and thereby reduce dynamic deformation. In addition, many large mirrors for ground and spaced-based telescopes utilize a multi-layer approach, sometimes with vertical stiffening members [15], or a honeycomb structure to maintain rigidity.

Mirror designs for obtaining optically flat polysilicon mirrors using SUMMiT V are described in this section. New techniques include trapping the sacrificial oxide between two polysilicon layers, adding vertical stiffening members between those layers, and a combination of the aforementioned methods in a variety of shapes and sizes to help control the overall curvature of the mirrors.

## 3.2 First Layout

As discussed in section 3, several factors must be considered when designing MEMS mirrors, including scattering and losses due to surface topography and change in focus due to curvature. As a result, design features were incorporated to minimize these contributions to overall system loss, including reduced number of etch release holes, non-periodic etch release holes, multi-layers, reinforced mirrors and low-stress gold films [16]. Mechanical structure and thin film material properties, particularly stresses and stress gradients, also directly affect the optical performance of MEMS mirrors. Complete removal of stresses from the micromachining process is not possible by its very nature. However, utilizing mechanical structures within the mirror to compensate for the stresses can produce very stiff and flat mirrors. A number of different stiffening approaches were pursued.

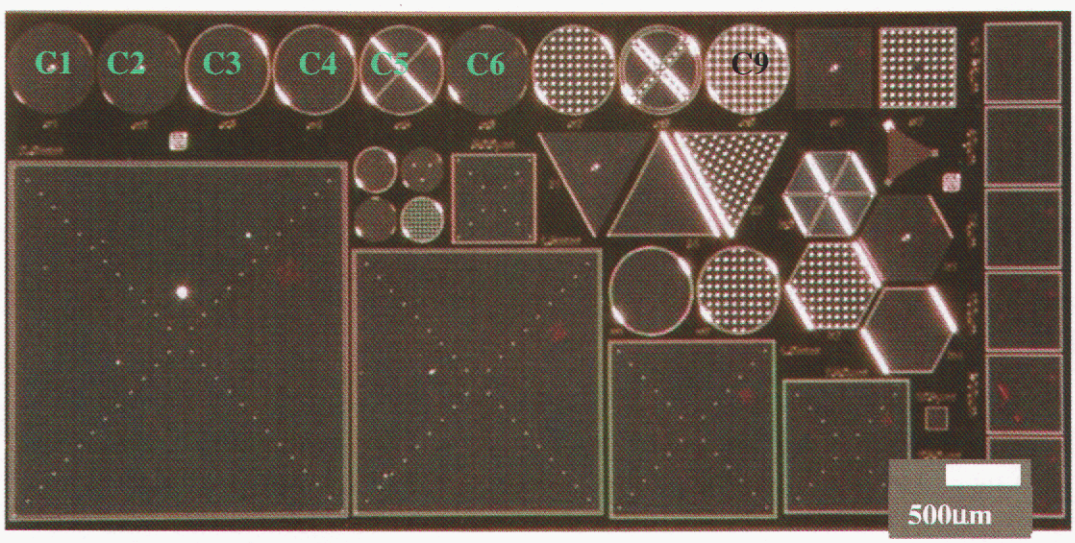


**Figure 8 Photomicrograph of initial mirror designs with Ti-Au coating. (designed by D.J. Dagel)**

The design approach for this study addresses the need for large diameter (>250 μm) mirrors with little or no bowing across their surface. For many optical applications, a mirror flatness of λ/20 is required, where  is nominally 550 nm (visible light). This criterion translates into a radius of curvature of 1 m for a 500 μm diameter mirror. Fig. 8 is a photomicrograph of the initial design layout displaying a variety of the design approaches, including mirrors with internal mechanical struts (vertical stiffening members) between polysilicon layers. In some cases, two polysilicon layers were laminated with no other mechanical reinforcement. Several mirrors are labeled which are discussed in Section 6.

Other mirror variations in the initial layout include varying size, ranging from 250 μm to 2 mm, mirror shape, including circular, square, triangular, and even hexagonal mirror structures, and finally thickness, consisting of different polysilicon laminate layers. The underlying structure was also evaluated to determine if a specific design would reduce print-though effects from the conformal nature of the fabrication process. Fig. 9 shows a 3-D view of one of the initial designs, a 500 μm mirror with an MMpoly3 mirror surface with a triangular underlying structure. Another mirror design variation includes encasing oxide in between polysilicon layers, which will be discussed in the next section of this section.

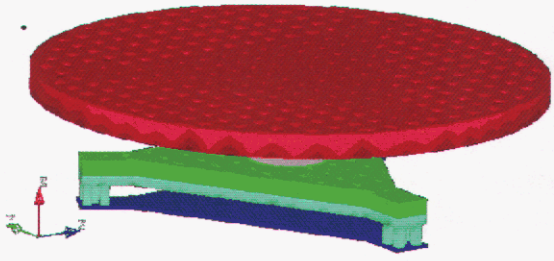

**Figure 9 500 μm MMpoly3 mirror (z-scale magnified).**

### 3.3 Mirror Redesigns

After the first layout was characterized, the possibility of an optically flat mirror was realized and new designs were created based on initial findings and modeling efforts. Figs. 10 and 11 show interferograms and 2-D cross sectional views of circular mirrors that illustrate several new design techniques. In both cases, the three-layer mirror is attached to a three-legged platform, which is anchored to the silicon substrate. In Fig. 10, the oxide layer trapped between the two polysilicon layers is nearly continuous across the entire mirror surface. Etch release holes allow removal of oxide beneath the mirror while leaving the oxide between the mirror layers (MMpoly3 and MMpoly4). As shown, the radius of curvature of this mirror is –0.3 m, which indicates a small convex profile. The oxide layer in Fig. 11, on the other hand, is trapped into several 50 μm-sized pockets in a checkerboard fashion. This design has two purposes: first, the sheet of oxide is separated into many small regions, thereby changing the overall stress characteristics; and second, the cuts between the oxide pockets fill with polysilicon, which creates vertical stiffening members and results in a honey-comb structure on the mirror. The design with the vertical stiffening members has, in contrast, a radius of curvature +0.9 m, which is slightly concave and very close to the desired curvature of ~1 m.

The fact that there is a difference in the sign of the radius of curvature shows that there is a possible way to produce optically flat mirrors beyond the λ/20 goal. If trapping oxide across the entire mirror surface as in Fig. 10 results in a negative curvature and doing so on a much smaller

length scale as in Fig. 11 results in a positive curvature, then it is probable that trapping oxide in areas somewhere between these two extremes will generate a mirror with essentially no curvature.

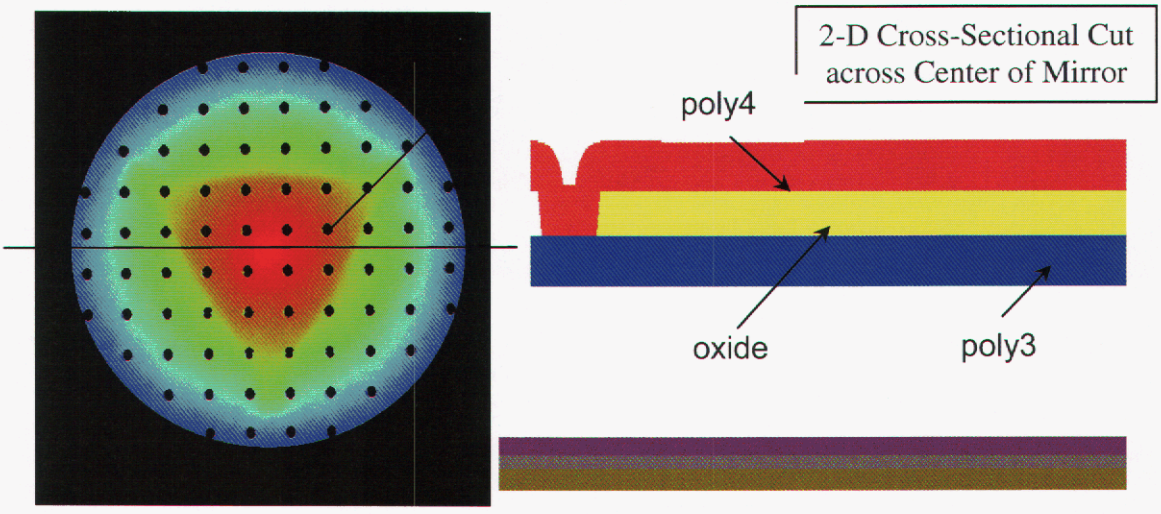


**Figure 10 a) Interferogram of 500 μm diameter mirror. Black dots are etch release holes for the oxide underneath the mirror and the triangular pattern is print-through topography from the support platform. The radius of curvature is -0.3 m. B) The mirror consists of an oxide layer between two polysilicon layers.**

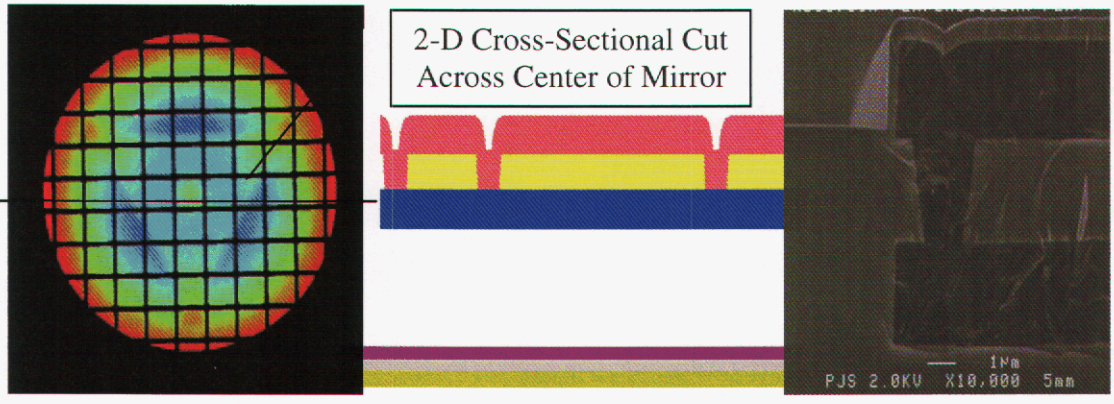


**Figure 11 a) Interferogram of 500 μm diameter mirror. the radius of curvature is +0.9 m b) the mirror has an oxide layer sandwiched between two polysilicon layers, only now the oxide is trapped in smaller regions c) SEM of mirror, detailing surface topography.**

Besides the trapped oxide region area, another variable that can be used to attempt to reduce curvature is the shape of the trapped region. Fig. 12 shows three possibilities from the second design layout. As a result of the high residual stress in the sacrificial oxide (~300 MPa), the oxide layer dominates the overall stress profile of a mirror with trapped oxide and explains why changing its extent and frequency varies the curvature significantly. By searching the design space through characterization and modeling, the optimum trapped oxide pattern (size and shape) will be found.

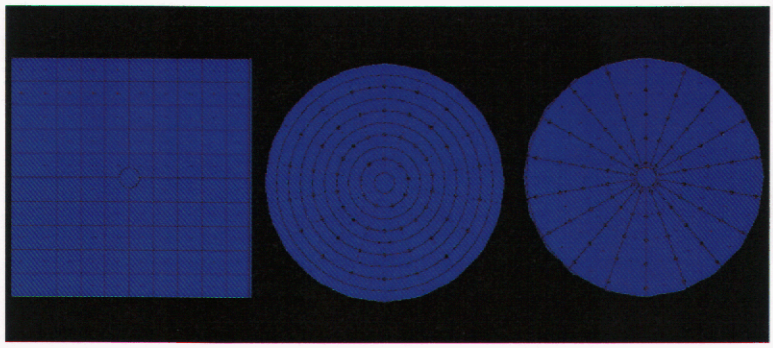

**Figure 12 500 µm mirror designs with trapped oxide in square regions (left), concentric rings (center), and polar slices (right). The trapped oxide area can be varied by changing the spacing of the cuts.**

It should be noted that when trapping oxide in the structure, additional surface topography is generated on the surface of the mirror (See Fig. 13). This optical problem can be reduced by making the oxide cuts as narrow as possible (1 µm) as illustrated in Fig. 14, where the conformal deposition essentially fills in the holes created by the oxide cuts.

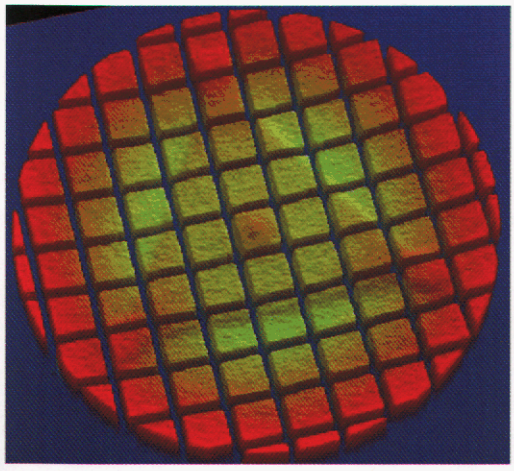

**Figure 13 Adverse topographical effects from trapped oxide in 500 µm mirror.**

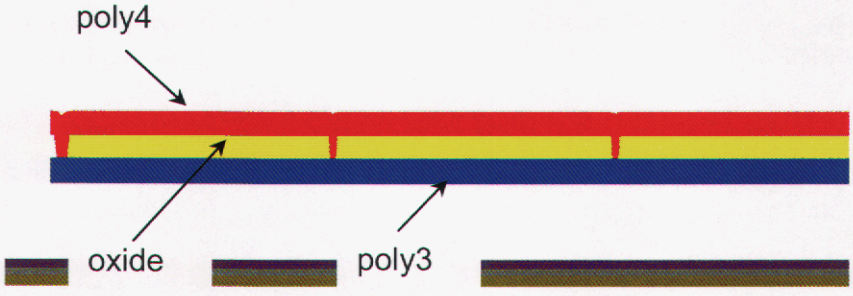


**Figure 14 Trapped oxide mirror where the oxide cuts have been made as narrow as possible to minimize surface topography. The perimeter cut is 2 µm wide, while the interior cuts are 1 µm wide.**

The second design layout is shown in Fig. 15. There are many different mirror designs, many with corresponding beams of similar length or mechanical structure. In order to better understand mirror curvature, single layer designs analogous to fixed-fixed and cantilever beams were fabricated in MMpoly3 and MMpoly4. These structures contain a single post in the center of the mirror plate or a thin ring supporting the outside edge like a drum. These designs are not intended to minimize curvature; rather, they are important for correlating mirror deflection and beam deflection. The characterization of these mirrors is discussed in Section 5. Several designs are labeled, which are discussed in Section 6.

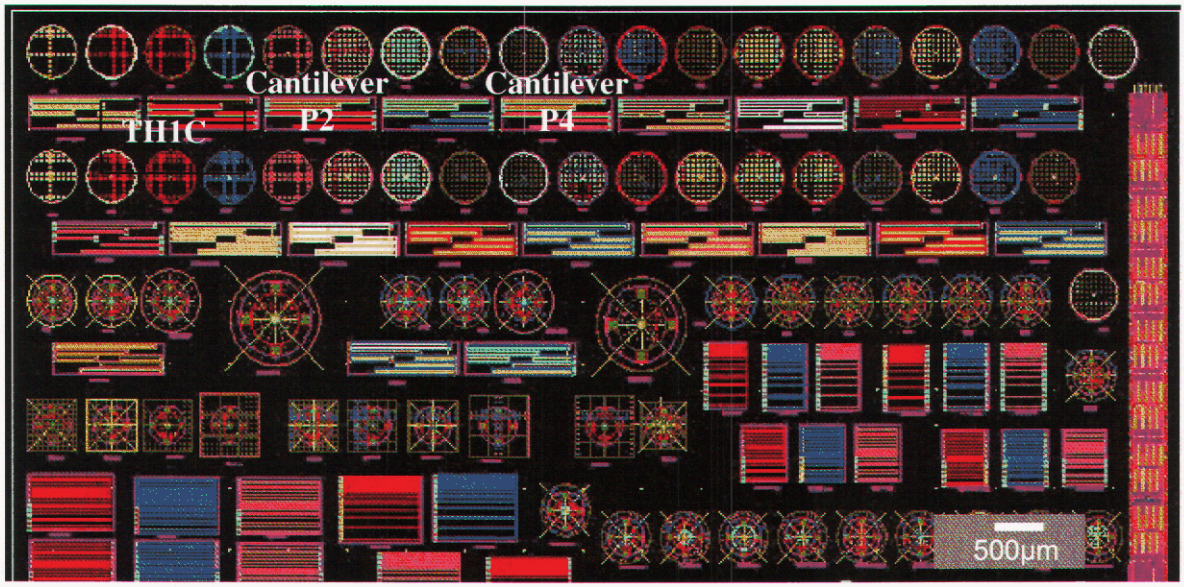


**Figure 15 Second mirror layout including beams & mirrors. (designed by D.J. Dagel)**

It should be noted that the process of designing an optically flat mirror is not necessarily a straightforward task. The characterization and modeling effort allow for a relatively quick analysis of many different design possibilities in comparison to an empirical approach of design, process, and characterize until one of the mirrors fits the design requirements. The characterization and modeling efforts are discussed in Sections 5 and 6, respectively.

### 3.4 Redesign #2

Arrays of mirrors of various designs aimed at optimizing their mirror figure were implemented in redesign #2. These are shown in Fig. 16. As can be seen, various mirror configurations are repeated in smaller, 5x5 sub arrays with a high fill factor. This is typical of imaging applications, where extremely high fill factors are required. Such high fill factors present unique challenges to fabrication as we found out on this reticle set. We found that the mirror flatness was best when solid MMpoly3 and MMpoly4 layers were interconnected by various shape and density of sacox4 cuts. Figure 17 illustrates how the mirror curvature degrades as function of decreasing MMpoly3 area. However, large pattern density in MMpoly3 layer caused a problem with CMP of the sacox4 layer. This is due to the fact that CMP thickness varies dramatically (as much as ~50%) with the under laying poly pattern density, which then causes the sacox4 etch to not reach deep enough to anchor MMpoly4 to MMpoly3 in places where sacox4 was thicker then anticipated.

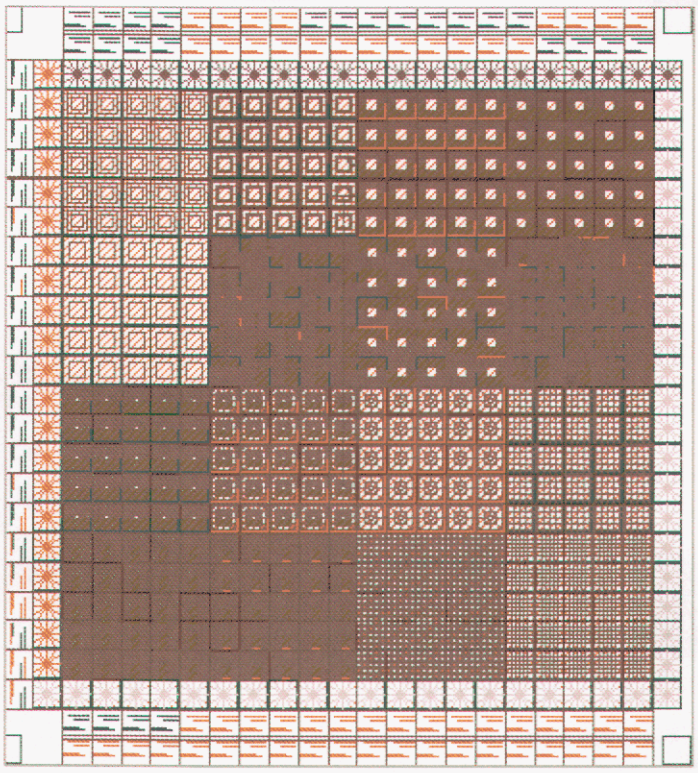

**Figure 16 Image of re-design #2 reticle showing in green mirrors remaining in place after release.**

This is what happened on our reticle. Due to insufficiently deep sacox4 cut, most of the mirrors in the center of the reticle (where pattern density is the highest and thus sacox4 is the thickest) floated off in release, because sacox4 cut did not reach to MMpoly3 to anchor them.

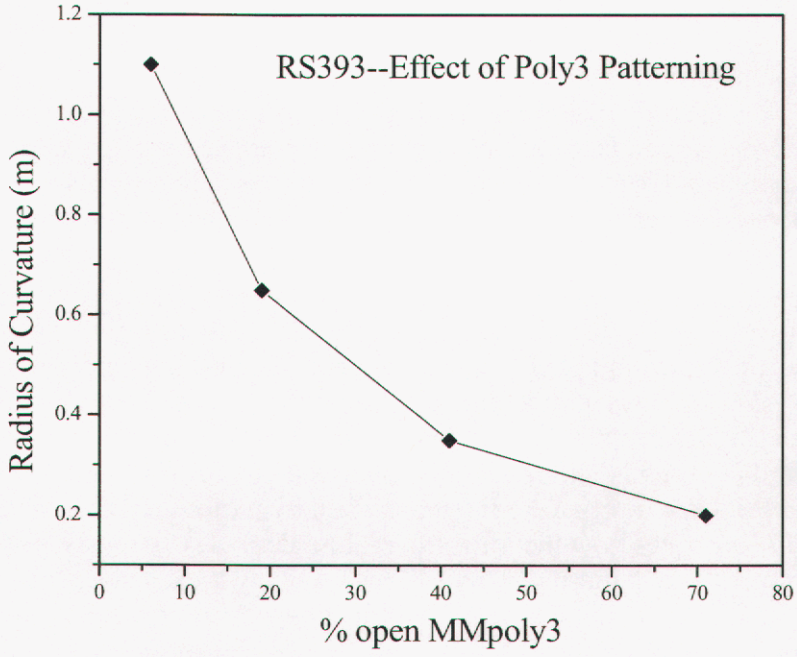


**Figure 17 Effect of reduced MMpoly3 area in an MMpoly3/4 laminate interconnected by sacox4 grid cuts on overall mirror radius of curvatur**

Figure 16 shows the areas where mirrors survived in green. The way this problem can be dealt with involves a block out procedure, oxide is etched back with a Reactive Ion Etch (RIE) to reduce the overall density of the topography and subsequent CMP processing produces less thickness variations over the surface of the wafer and locally. This is painful since it requires another mask level. Another approach requires monitoring sacox4 cut etch depth in the area of maximum pattern density and therefore oxide thickness (i.e. middle of the array, rather then diagnostic region) and etching as long as necessary to reach MMpoly3. As seen in Figure 17, in order to obtain mirrors with a large radius of curvature, both MMpoly3 and MMpoly4 must be solid and only the sacox4 cuts can vary. This of course is not an ideal solution because MMpoly3 layers cannot be used for actuator structure since they are employed in stiffening the mirror. We hypothesize that since MMpoly3 and MMpoly4 have the opposite stress gradient, they act to balance each other out.

# 4 Characterization of Beams and Mirrors

Much work has been put into characterizing MEMS structures [17-36]. This effort indicates the great need for such material properties in both analysis and design. In order to gain an understanding of the mechanical properties in the polysilicon layers in this study, simple beam and mirror test structures were measured to extract these properties. The test structures include MMpoly12, MMpoly2, MMpoly3, and MMpoly4 cantilever beams, fixed-fixed beams of various lengths and widths, and round mirrors both fixed by a central post and fixed on the other edge. This study focused initially on simple beam structures, including cantilevers and fixed-fixed beams to gain an understanding of the stress gradients and residual stresses in the polysilicon. Then large plate, i.e. mirror structures, were designed and studied to evaluate residual stresses and also to correlate the stress values of the simple beams and plate structures.

## 4.1 Interferometry

Because MEMS devices are extremely small, special techniques must be used in order to view their small scale features, typically on the order of nanometers. Interferometric microscopes were used to characterize the beam and mirror structures in this study. A typical Michelson Interferometer is shown in Fig. 18. Precise measurements of the MEMS structures can be made with the interferometer. The interferometer is an optical device that divides a beam of light exiting a single source into two beams and then recombines them to create an interference pattern due to a difference in phase [37]. The interference is constructive at some points and destructive at others, which causes an interference fringe pattern to form. This interferogram can then represent the surface topography of the MEMS device.

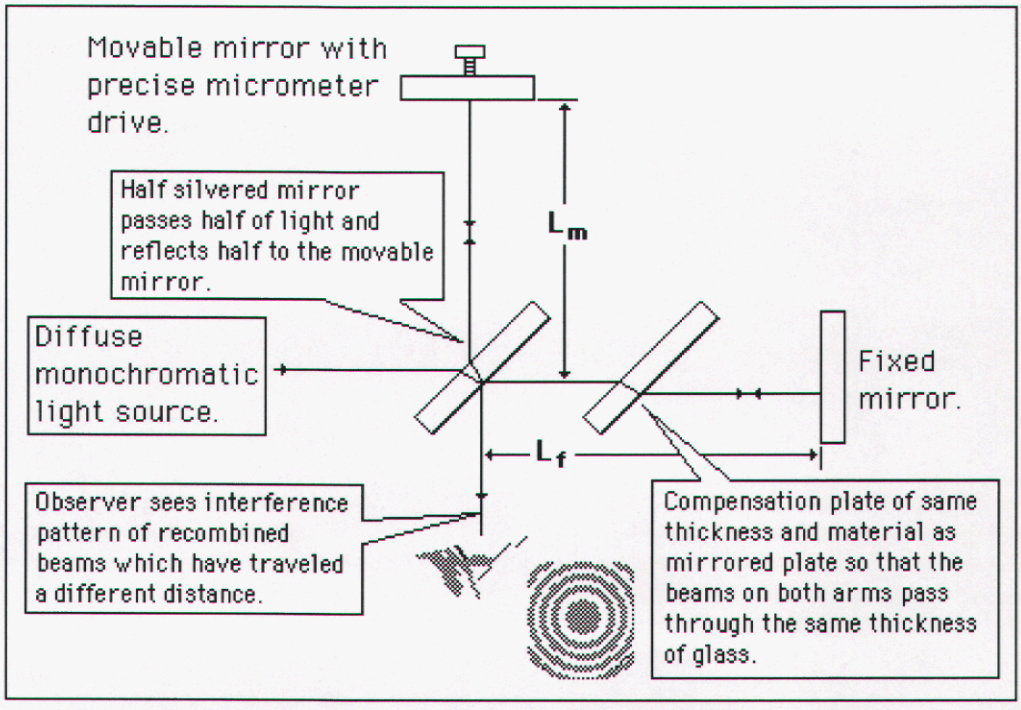


**Figure 18 Michelson interferometer system [38].**

### 4.1.1 WYKO, Sandia Laser Interferometer, ADE Phase Shift MicroXAM

During the course of this research, several interferometers were used to validate data. Most of the data acquired was from a WYKO NT3300 white-light interferometry system. However, a Sandia created green light laser interferometer was used for verification of beam measurements and an ADE Phase Shift MicroXAM interferometric microscope was used for initial measurements of the metallic coatings covered later in this section.

The WYKO interferometer is a powerful tool, enabling a fully automatic stage control and the capability to automate measurements. There are several different modes in which to measure and it is important to note the differences between vertical scanning interferometry (VSI) mode and phase shifting interferometry (PSI) mode. VSI enables a long scanning range of 2 mm but has a limited resolution of 3 nm. The PSI mode includes a high resolution of 3 Å though it is limited by the need for small step-heights, continuous slopes and a scanning range of less than 160 nm. In order to visually explain these features, Fig. 19 shows a 3-D mirror surface in both VSI (a) and PSI (b) modes. The topographical features (vertical stiffening members) are exaggerated in the PSI mode due to a different scale and scan range. The mechanical reinforcements are seen as large trenches, and the underlying support structure can also be seen as print-through topography due to the high resolution in PSI mode.

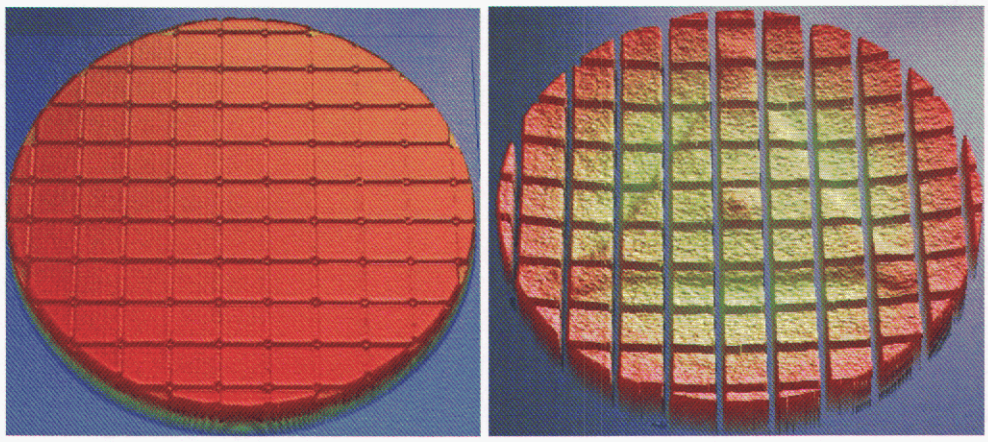

**Figure19. 3-D Interferograms of reinforced 500 µm mirror with roc: +0.9 m (a) VSI mode (b) PSI mode.**

Both PSI and VSI modes are routinely used in this study, each mode having appropriate features for different circumstances. PSI mode is used when detail of the mirror surface is needed, yet VSI mode is used when a structure needs to be leveled to the substrate, which is the case in most beam measurements.

Also of note in this study is the comparison of white-light (full spectral colors) for VSI mode or filtered red light (632 nm) in PSI mode, or filtered green light (~502 nm) measurements. Polysilicon MEMS structures are semi-transparent to visible light, which allows secondary fringes to appear on the underside of the polysilicon layer when white-light is used. The actual measurement will show these secondary fringes and the uniformly curved beam will look wavy. This secondary fringe behavior will cause the automated curve fitting subroutine in the WYKO software to calculate the surface incorrectly. These issues of secondary fringes prompted a study of white-light vs. green light interferometry methods. Several measurements were taken on both the white light WYKO and green light laser interferometer using the same MEMS devices. The results of the study indicated the need for a green filter on the WYKO system to reduce secondary fringes in measurements. All measurements presented were obtained using a green light filter.

## 4.2 Beams

As discussed earlier in Section 3, several factors are considered when designing MEMS mirrors, including light scattering and losses due to surface topography and change in focus due to curvature. The curvature in polysilicon MEMS devices is a direct result of the residual stress and stress gradients through the thin film. Surface-micromachined thin films possess a fair amount of residual stress (~MPa). After removing the sacrificial oxide layers used to mechanically and electrically separate the structural polysilicon layers, the MEMS structures deform in proportion to the magnitude and sign of the residual stress. The resulting deflections can be predicted by measuring the stress profiles of each layer and by entering this data into the appropriate equation or model. Given the complexity of the SUMMiT process, understanding how stress affects non-standard designs is a difficult challenge. Fig. 20 shows the SUMMiT diagnostic regions next to 2820 μm x 6340 μm modules, where test structures such as fixed-fixed and cantilever beams are located, which are routinely measured for material properties. Fig. 21 shows a scanning electron micrograph (SEM) of a set of cantilever and fixed-fixed diagnostic beams, where the longest fixed-fixed beam is 800 μm long.

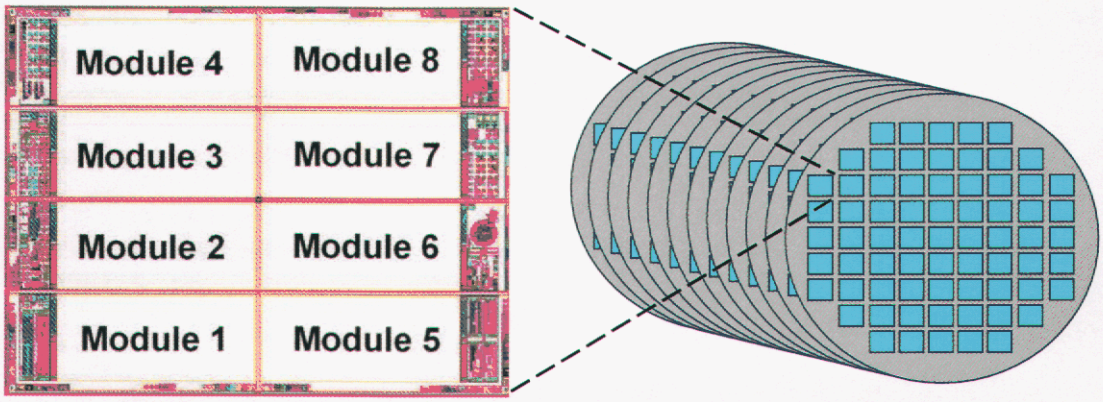


**Figure 20 Detail of wafer level to module and location of diagnostic structures. [29]**

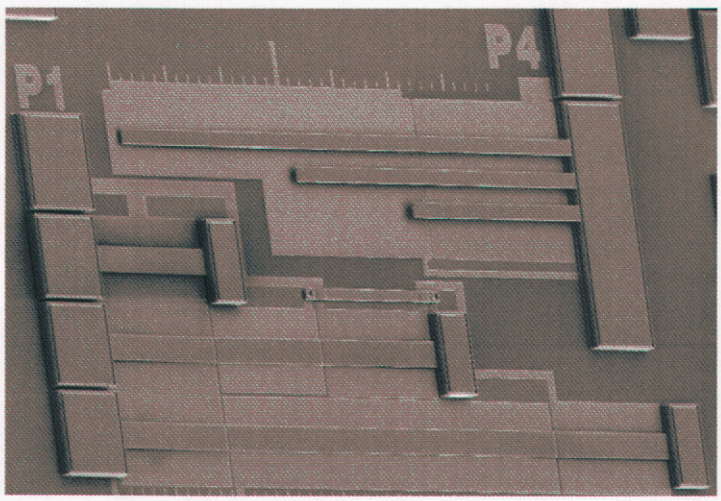


**Figure21 SEM of diagnostic region from SUMMiT process.**

In Fig. 22, a portion of the second layout created in this study is shown, which displays the additional cantilever and fixed-fixed beams placed near the mirror structures, to verify that stress data gathered is as accurate as possible since there is some variation of stress values across a

wafer [32]. In the next several sections, the cantilever beams and fixed-fixed beams will be discussed in relation to how they correlate material properties such as stress gradient and residual stress, respectively.

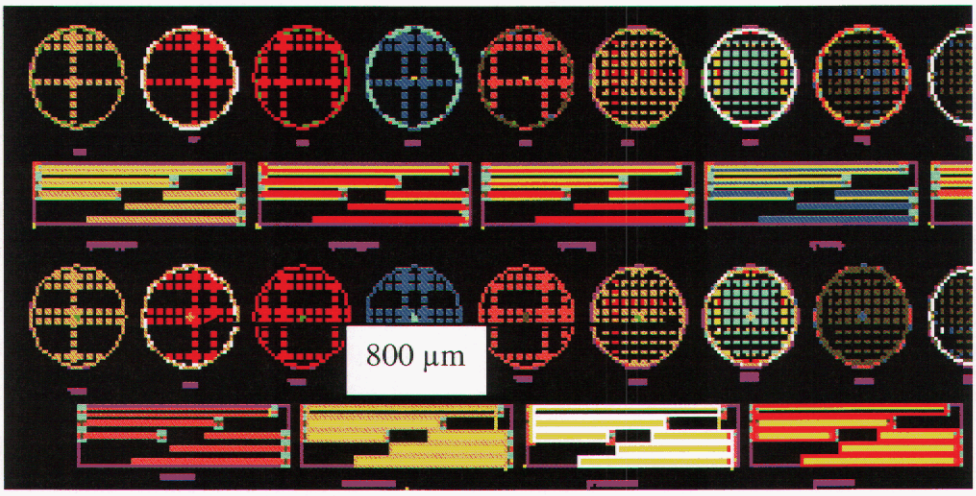


**Figure 22 Portion of second layout displaying detail of 500 µm mirrors & beam correlations.**

### 4.2.1 Beam Theory: Cantilever Beams

To better understand the role of thin film stress gradients in the multi-layered SUMMiT structures we have measured the radius of curvature of several cantilever beams in those layers. Deflection values and shapes were measured optically with a WYKO interferometric profiler. A sample of measured results is shown in Fig. 23, where the cantilevers are 200 µm to 1000 µm long. The radius of curvature is automatically calculated from the optical profile and related to the stress gradient through calculations shown below.

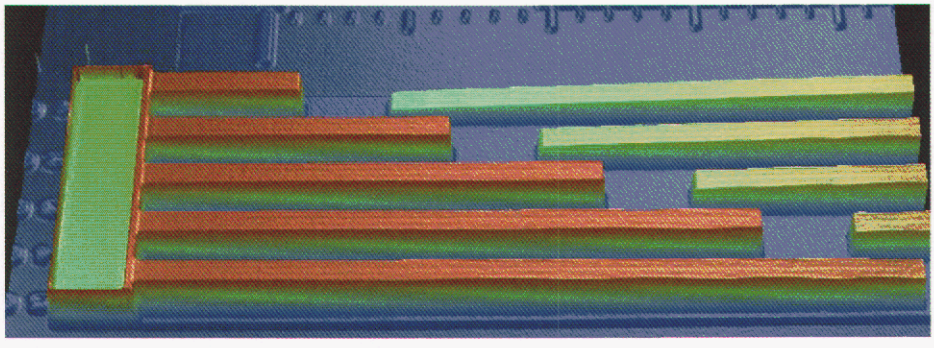

**Figure 23 3-D interferogram of cantilever beams generated by interferometry.**

The radius of curvature of a cantilever beam can be approximated through geometrical relationships as follows:

$$\rho = \frac{L^2}{2B} \tag{4.1}$$

where L is the length of the cantilever, and B is the peak-to-valley bow [39].
In order to analyze the beams, the stress states before release, directly after release, and after the beams bend must be taken into consideration. Before release, the beam material has an average

compressive stress and also a stress gradient that result from the deposition. Once the processed parts are released, the beam length increases slightly to relieve the compressive stress so that the average stress goes to zero; however, the stress gradient remains. The stress gradient is calculated from the following equation:

$$\frac{\sigma_1}{t} = \frac{1}{2}\left(\frac{E}{1-\nu}\right)\frac{1}{\rho_x} \tag{4.2}$$

where t is the thickness of the beam, $\rho_x$ is the radius of curvature, E is Young's Modulus (164 GPa used in this study [17]), and ν is Poisson's ratio (a value of 0.23 was used for polysilicon) [Appendix A].

Fig. 24 depicts multiple cross-sectional profiles through the length of MMpoly3 and MMpoly4 cantilever beams. These plots show some variability, but still have a fairly consistent curvature. The plot in Fig. 25 shows a quarter-wafer map plot of MMpoly3 and MMpoly4 cantilever beam curvature data. The statistical standard deviations are 0.00287 m and 0.01297 m respectively, which indicates that the curvature, and thus, stress gradient does not vary much across the wafer.

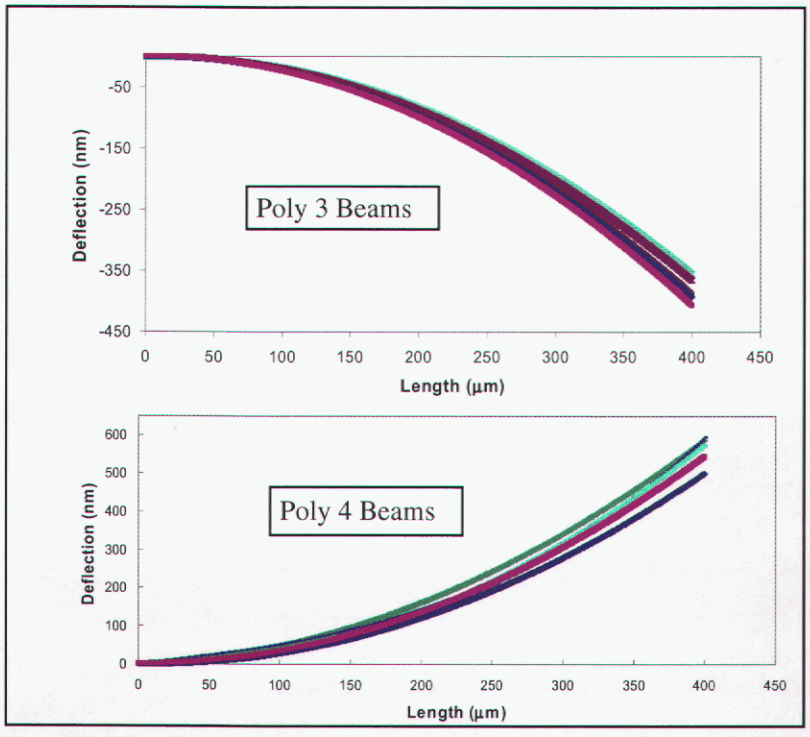


**Figure 24 Interferometric deflection curve data for MMpoly3 and MMpoly4 cantilever beams.**

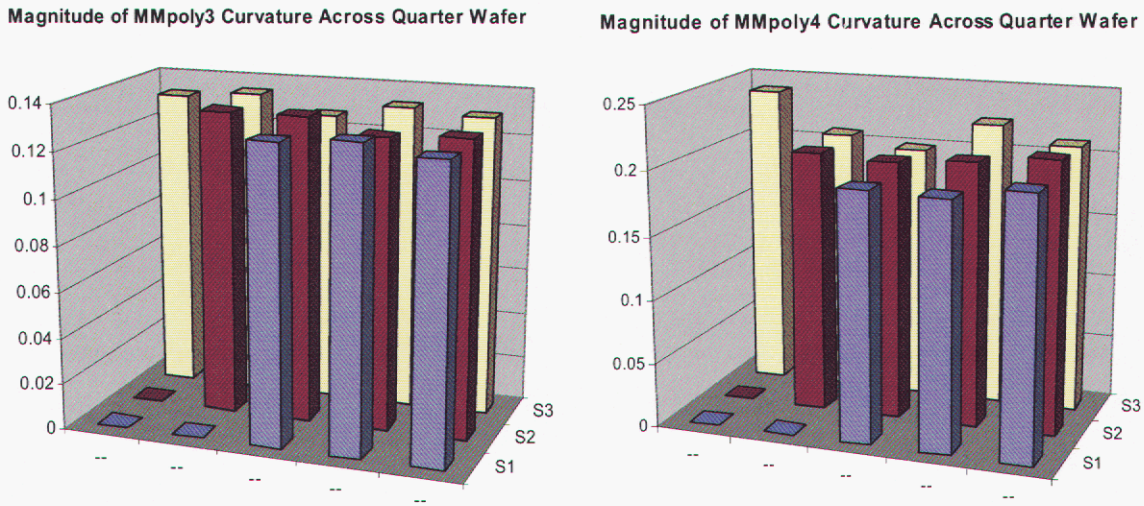


**Figure 25 Quarter wafer plot of curvature for MMpoly3 and MMpoly4.**

### 4.2.2 Beam Theory: Fixed-Fixed Beams

To understand the role of residual stresses in the multi-layered structures, buckled deflection of fixed-fixed beams in those layers must be measured. Deflection values and shapes were also measured optically with a WYKO interferometric profiler. The buckled deflection of a 600 μm long fixed-fixed beam can be seen in the scanned optical profile in Fig. 26 (the other beam is 400 μm long) and is related to the residual stress through calculation.

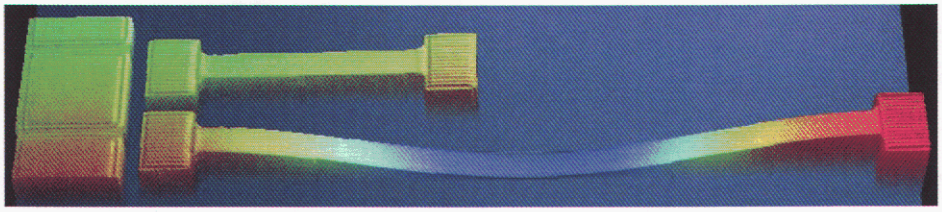

**Figure 26 Fixed-Fixed beams as visualized with interferometry.**

Beams supported at both ends with axial constraints have net residual stresses. Due in part to thermal effects, external axial loads or other residual stress effects, these stresses significantly affect the beam bending behavior. When these residual stresses cause the beam to buckle, or exert an out-of-plane deflection, residual stress can be calculated from the observed beam deflection. Residual stress in fixed-fixed beams is calculated from the following equation:

$$\sigma_{res} = \frac{E\pi^2}{L^2(1-\nu)}\left(\frac{t^2}{3}+\frac{c^2}{4}\right) \tag{4.3}$$

where E is Young's Modulus, ν is Poisson's ratio, t is the thickness of the beam, c is the amplitude of deflection, and L is the length of the beam [Appendix B].

### 4.3 Plates (Mirrors)

In order to better understand mirror curvature, single layer designs analogous to fixed-fixed and cantilever beams were fabricated in MMpoly3 and MMpoly4. These structures contain a single post in the center of the mirror plate as depicted in Fig. 27 or a thin ring supporting the outside edge like a drum, Fig. 28. These designs are not intended to minimize curvature; rather, they are important for correlating mirror deflection and beam deflection.

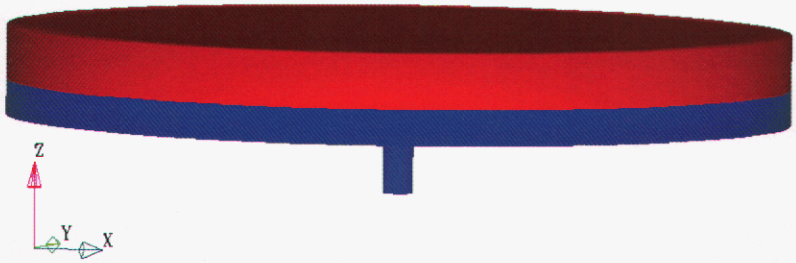


**Figure 27 MMpoly12 500 µm mirror with center post support.**

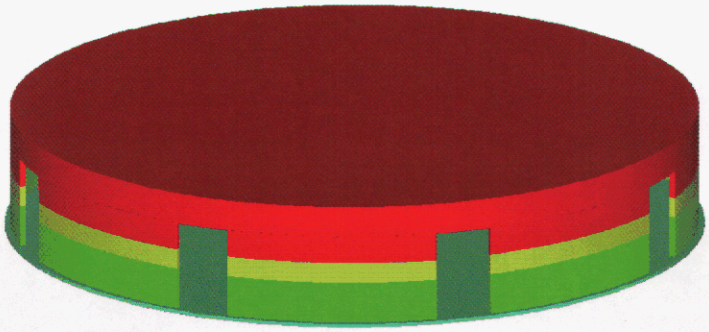

**Figure 28 MMpoly3 500 µm mirror with outer ring supports.**

As mentioned in section 4, the second layout incorporates several mirrors with different arrangements of trapped oxide as shown in Fig. 29. Displayed in Fig. 30 is a graph of measured data for the mirror deflection as a function of trapped oxide in a variety of different shapes. There is a definite trend for all oxide shape types showing a much greater deflection with a higher percentage of trapped oxide. Having a high concentration of trapped oxide is not ideal due to the high residual stress in the oxide (~300 MPa).

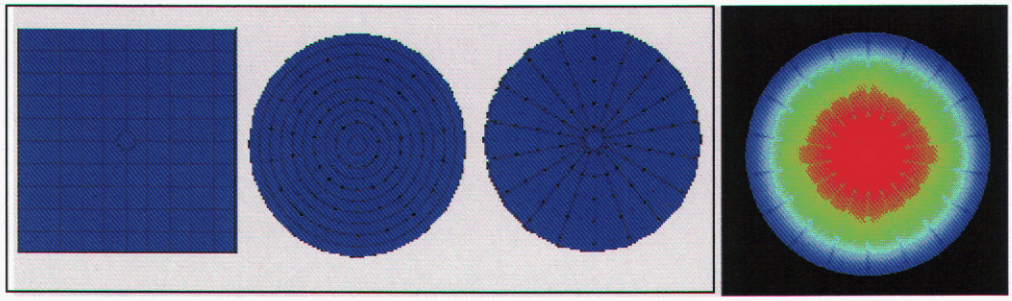

**Figure 29 a) Designs with trapped oxide in square regions (left), concentric rings (center), and polar slices (right). b) interferogram of polar slices mirror.**

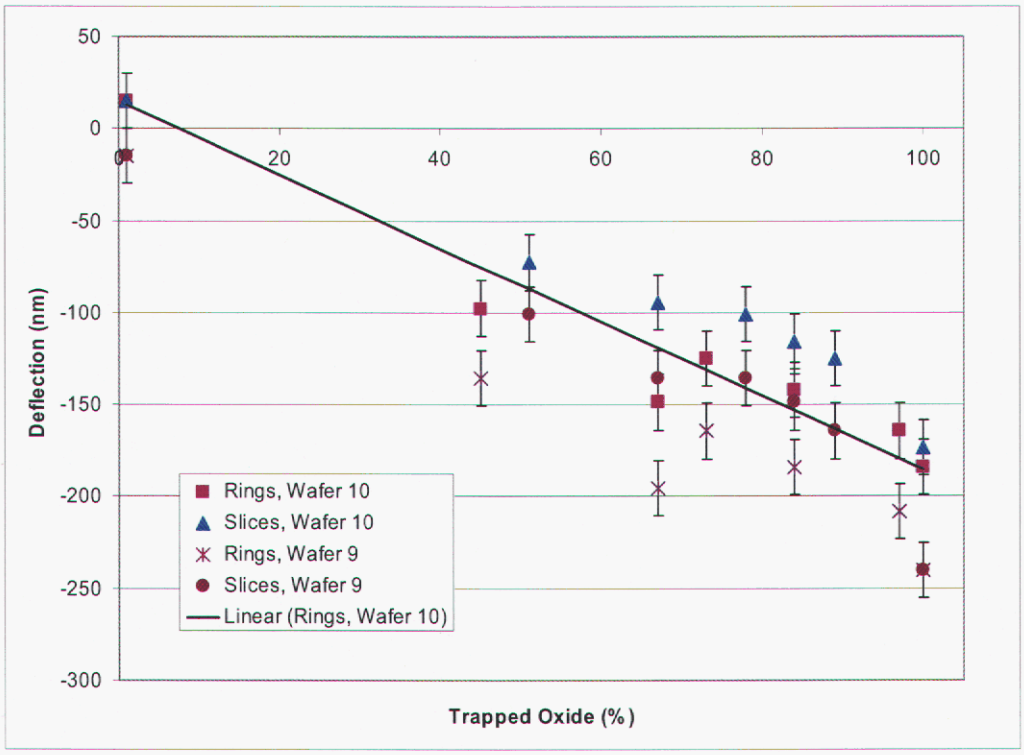


**Figure 30 Mirror deflections as a function of trapped oxide for a variety of shapes.**

Fig. 31 depicts data of radius of curvature as a function of SacOx4 cut spacing for a variety of different shapes. The MMpoly3, MMpoly4 and MMpoly3 & 4 laminate lines are given to show typical radius of curvatures for those arrangements. When the cut spacing increases, the ring shapes with no oxide, square shapes with no oxide and slices with no oxide exhibit behavior of a decrease in radius of curvature. This trend indicates that these types of arrangements benefit from a smaller SacOx4 cut spacing, thus a thicker polysilicon layer. This graph also shows that the radius of curvature can be greater than 1 m with just mechanical reinforcements, which is much better than an MMpoly3 & 4 laminate.

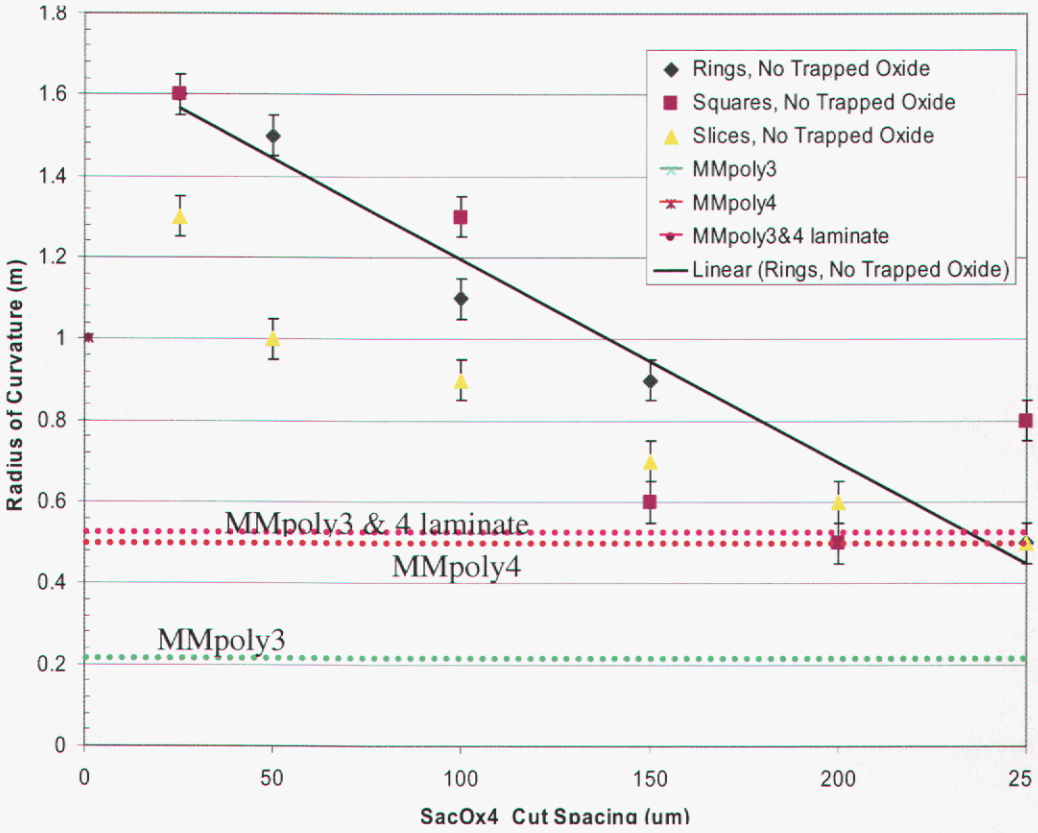


**Figure 31 Mirror radius of curvature as a function of sacox4 cut spacing for a variety of shapes.**

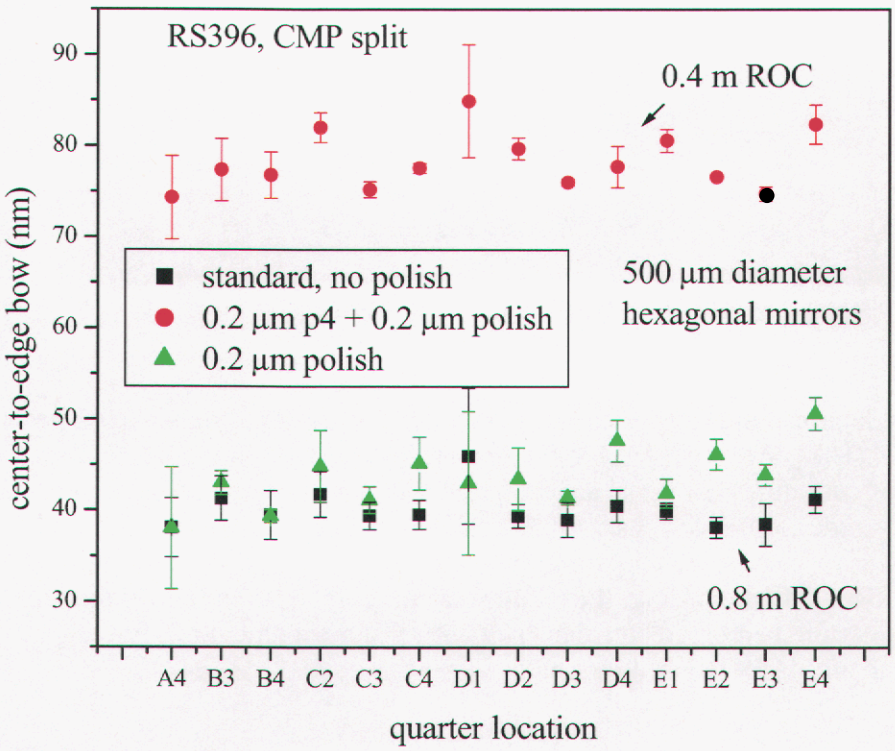


**Figure 32 Mirror radius of curvature as function of different surface treatments.**

We also investigated the effect of CMP on both print through and mirror curvature. Several splits of the second design were carried out where the final layer of poly was subjected to CMP where 0.2 μm of poly was removed, thickened by 0.2 μm and then had the additional thickness removed by CMP and finally one split was left in a standard state (i.e. no thickening, no CMP). Figure 32 illustrates the outcome of this experiment showing the center-to-edge bow (and corresponding radius of curvature) for 500 μm hexagonal mirrors with different surface treatments. What is observed is CMP appears to impart additional curvature (this is especially evident in the case of thicker MMpoly4 – for the case of standard poly thickness and removal of 0.2 μm of poly by CMP, radius of curvature appears to be unchanged from the standard case – but that could be due to thinner final poly layer). So it would appear not to be a good idea to CMP the top layer of poly. However, CMP does do a very good job of removing topography due to sacox4 cuts. As shown in Figure 33, CMP reduced topography due to sacox4 cut from 70 nm (a) to less then 10 nm (b):

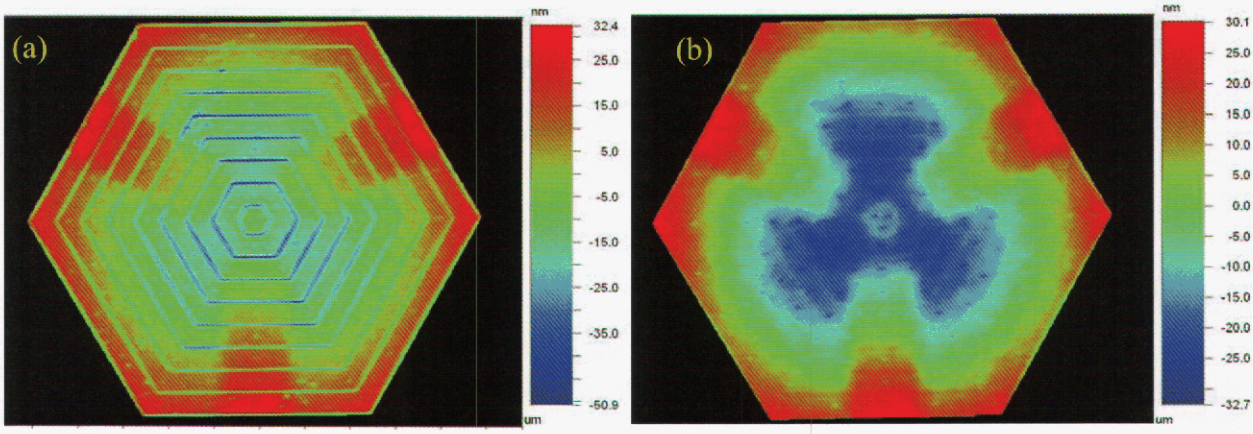


**Figure 33 Interferometric images of hexagonal mirror surfaces a) no CMP finish on MMpoly4 (standard) b) CMP on MMpoly4**

# 5 Modeling and simulation of mirror figure

Finite element modeling provides an inexpensive alternative to empirical designing when taking into account the total time and cost of fabrication. Modeling of MEMS devices is beneficial to the designer, given that foundry turnaround times are on the order of several months. Pre-fabrication analysis allows the designer to determine how his device or system will behave under many different cases without ever having to build a structure. In order for the modeling effort to be productive, it must begin with a good understanding of the fabrication parameters and any process variations or limitations. These parameters, which are essential to the success of understanding the design include, but are not limited to, residual stresses, stress gradients, layer thicknesses, pattern density, and wafer curvature. It is important to have bounds for these parameters for initial modeling, although exact values are needed after fabrication of the devices in order to validate results.

This study describes finite element analysis (FEA) modeling tools used in the design phase of optical MEMS. Current modeling tools are useful for design verification, but are not often used in the early phases of design [40], although, this work shows that FEA modeling can be used as a predictive design tool.

This section will first cover analytical modeling methods for simple structures. Analyses will include both cantilever and fixed-fixed beams and plates (mirrors). Numerical analysis techniques will be discussed and CoventorWare [41], the FEA code used in this study, will be detailed with several modeled results.

## 5.1 Analytical Modeling

Analytical analysis allows the designer to get an initial solution for a problem in a timely manner and in most simple structural cases these results are quite accurate, although they break down for complex structures. First, cantilever beams, fixed-fixed beams and then plate analytical solutions are covered in this section.

### 5.1.1 Beams

The discussion in section 4 covered how to characterize beams using the stress gradient and residual stress analytical equations. The approach in this section is to display basic elements for beam deflection equations for cantilever and fixed-fixed beams.

#### 5.1.1.1 Beam Deflection Theory: Cantilever Beams

Cantilever beams (Fig. 34) are fixed at one end and free at the other, which allows both force and moment reactions at the fixed support. The free end may translate or rotate, which is why the MEMS cantilever beam structures (Fig. 35) discussed in section 4 curve due to the distributed stress gradient through the beam thickness.

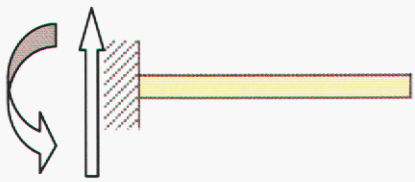

**Figure 34 Cantilever beam: fixed at one end, free on the other. Force and moment reactions at the fixed support are shown.**

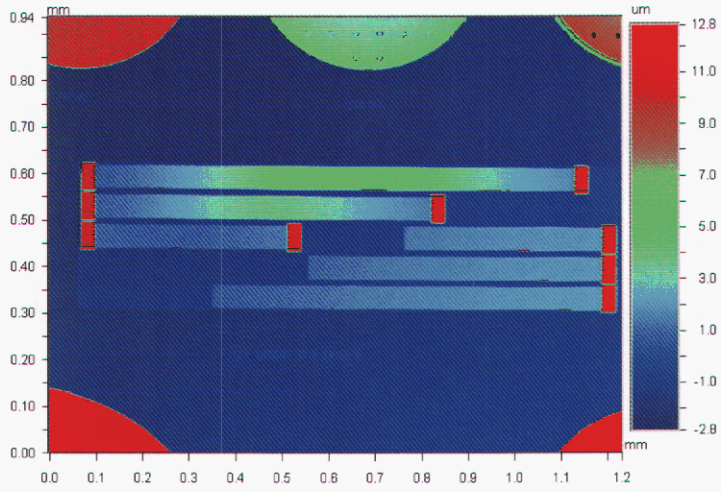


**Figure 35 2-D interferogram of MEMS fixed-fixed and cantilever beams (400 µm-800 µm long).**

When a beam is loaded, the initially straight beam is deformed into a curve, called the deflection curve of the beam. For a cantilever beam with a continuous load across the length of the beam (Fig. 36), the shape of the curve is governed by the differential equation of the deflection curve. Equation 5.1 gives the differential equation which relates the curvature to the deflection of the beam.

$$\kappa = \frac{1}{\rho} = \frac{\partial \theta}{\partial x} = \frac{d^2 \upsilon}{dx^2} = -\frac{M}{EI} \tag{5.1}$$

where κ is the curvature, equal to the reciprocal of the radius of curvature ρ, θ is the angle of rotation, υ is the deflection, M is the moment applied, E is Young's modulus, and I is the moment of inertia of the beam [42].

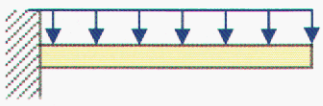

**Figure 36 Cantilever beam with continuous loading across surface.**

For a cantilever beam with a continuous loading, q, across the surface of the beam, the deflection and angle at the free end of the beam is calculated to be:

$$\delta_b = \frac{qL^4}{8EI} \quad \text{and} \quad \theta_b = \frac{qL^3}{6EI} \tag{5.2}$$

where L is the length of the beam before deflection [42].

### 5.1.1.2 Beam Theory: Fixed-Fixed Beams

Fixed-fixed beams are statically indeterminate, which indicates that the beam has a larger number of force and moment reactions than can be found from equations of static equilibrium. The fixed-fixed beam is constrained in some fashion on both ends as shown in Fig. 37. Although, the MEMS beam is not completely rigid on both ends; there is still a dependence on the compliance of the anchor. This study does not fully consider the effects of the beam take-off angle [43-49]. The out-of-plane displacement (see Fig. 38), w of a beam is governed by the Euler-Bernoulli beam equation:

$$\frac{d^2}{dx^2}\left[EI\frac{d^2w}{dx^2}\right] = p \tag{5.3}$$

where E is Young's modulus, I is the area moment of inertia of the beam's cross section, w is the out-of-plane displacement, and p is the distributed loading (force per unit length) acting in the same direction as w [50].

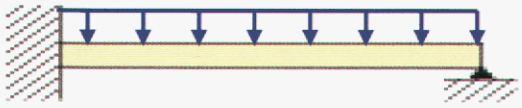

**Figure 37 Fixed-simply supported beam**

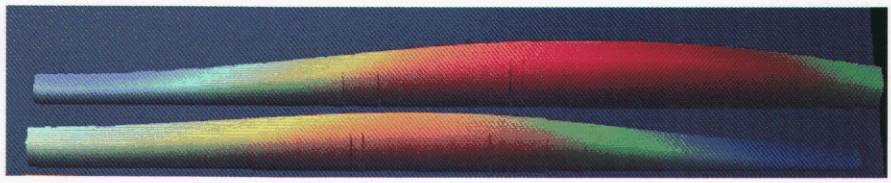

**Figure 38 3-D interferogram of two buckled fixed-fixed beams (600 µm & 800 µm long).**

For a fixed simply supported beam with a continuous loading, q, across the surface of the beam, the deflection at the center of the beam is calculated to be:

$$\delta_b = \frac{5qL^4}{384EI} \tag{5.4}$$

where L is the length of the beam before deflection [42].

### 5.1.2 Plates (Mirrors)

The use of plate theory is appropriate for the analysis of micromachined thin-film mirror structures. Small plate deflection theory is often used for deflection less than 1/5 of the layer thickness. Large deflection plate theory [51-53] is used for deflections up to three times the layer thickness [51]. The structures in this study exhibit both small and large deflection theory characteristics; however, only small deflection theory will be covered in this section.
The small out-of-plane displacement w of a thin plate is governed by the classical plate equation:

$$\nabla^2 D \nabla^2 w = p \tag{5.5}$$

where $p$ is the distributed load (force per unit area) acting in the same direction as $z$ (and $w$), and D is the bending/flexural rigidity of the plate defined as follows,

$$D = \frac{Et^3}{12(1-\nu^2)} \tag{5.6}$$

where $E$ is the Young's modulus, v is the Poisson's ratio of the plate material, and $t$ is the thickness of the plate [51].
The deflection w of a circular plate fixed on the outer edge under a uniform applied pressure P, is given by:

$$w(r) = \frac{\mathrm{Pr_0}^4}{64D}\left[1-\left(\frac{r}{r_0}\right)^2\right]^2 \tag{5.7}$$

where r and $r_0$ are the radial coordinate and plate radius, respectively and D is the flexural rigidity as defined earlier [53].

## 5.2 Numerical Analysis

This study uses finite element analysis (FEA) software for the numerical analysis of the mirrors. In FEA, the structure to be analyzed is discretized into small elements, each having its own stiffness matrix. There are several finite elements that have been developed to represent common structures and that will be discussed in this thesis, including tetrahedra elements (triangular), brick elements (rectangular), and hexahedra elements. These elements mathematically store the stiffness matrix in fundamental equations (Equation 5.8). Specific parameters such as distinct coordinates and material properties like Young's modulus, Poisson's ratio, and density are put into these elements, so that the local stiffness is uniquely known for that exact element. When a structure is fully discretized, or meshed, into many elements, its global stiffness can be found through the combined stiff nesses of all the other interacting elements. When a force or set of forces is applied to the structure, the displacement response can be calculated by inverting the global stiffness matrix, as displayed in the following equation:

$$[F] = [k][x] \rightarrow [x] = [F][k]^{-1} \tag{5.8}$$

where [F] is the applied force matrix, [k] is the stiffness matrix, and [x] is the displacement matrix.

This fundamental concept is used in the solution of many problems, including a variety of complex loading conditions, such as internally and externally applied forces, pressures, and temperatures. The finite element analysis technique will be used in the following sections to calculate parameters for the complex MEMS mirror structures where analytical approaches become very difficult.

#### 5.2.1.1 CoventorWare usage specifics

The first step in using FEM software is to simplify the geometry of the structure so it is convenient to mesh. It is ideal when the geometry is completely square, so that a brick or Manhattan element can be used to mesh the structure. This usually requires making unnecessary rounded edges square and removing small features like etch release holes. The removal of rounded edges and small etch release holes does not usually significantly affect the mechanical and electrostatic solutions for the structure. If these features are included, the number of nodes or degrees of freedom where the elements connect [54] on the structure and the calculations the processor has to compute increases significantly. However, most of the mirror structures modeled in this study are round, so the Manhattan brick elements are only used for the beam analysis.

In the case of more complex geometry like ours, a tetrahedra mesh or hexahedra mesh must be used. An MMpoly3 membrane mirror is shown in Fig. 39 with a tetrahedra mesh, compared with Fig. 40, which displays a hexahedra mesh on the same mirror. It should be noted that the tetrahedra mesh will usually mesh any geometry, but the element symmetry is sacrificed. This symmetry is important when analyzing deflection across a uniform mirror surface, given that if the mesh is offset, the deflection of the mirror will appear inconsistent and the results may be incorrect.

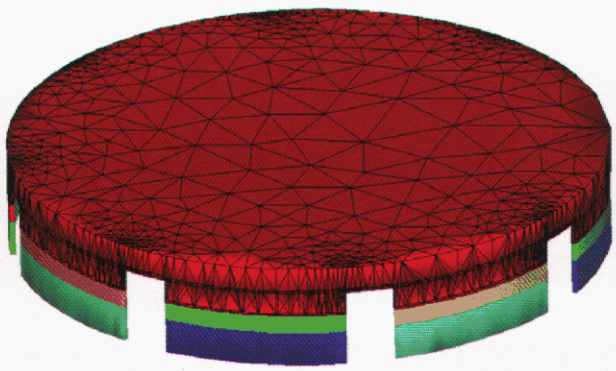

**Figure 39 MMpoly3 500 µm membrane mirror with tetrahedral mesh displayed.**

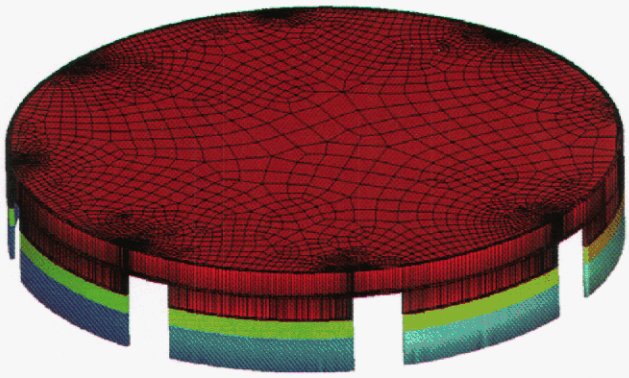

**Figure 40 MMpoly3 500 µm Membrane mirror with hexahedra mesh displayed; notice the mesh symmetry.**

After the geometry is created and meshed, boundary conditions are applied before solving for the deflection of the mirror or other parameters of interest. The mechanical solver in CoventorWare is called MemMech. The MemMech BC window allows the user to set the mechanical boundary conditions for the solver. To start any analysis, boundary conditions must be applied to the structural model. All mirror posts or rigid anchors attached to the substrate were fixed for no deflection in all three axes. Internal residual stress and stress gradient (see in section below) conditions were applied to all models in this study. These stresses are assumed to be constant throughout the material layer. When the run is completed, tabular results of total displacement or other specified parameters can be viewed.

### 5.2.1.2 Plates (Mirrors)

Finite element models were developed in this study to validate measured mirror deflection values of the mirrors. Modeled mirror deflection correlated well with interferometric results using the cantilever and fixed-fixed beam stress data gathered earlier. For example, the 500 µm diameter MMpoly3 mirror shown in Fig. 41 was modeled mechanically using only the boundary conditions of the measured beam residual stress and stress gradient data. The deflection solution for that mirror is shown in Fig. 42 and produced a radius of curvature of +0.19 m compared with +0.17 m measured with interferometry (Fig. 43).

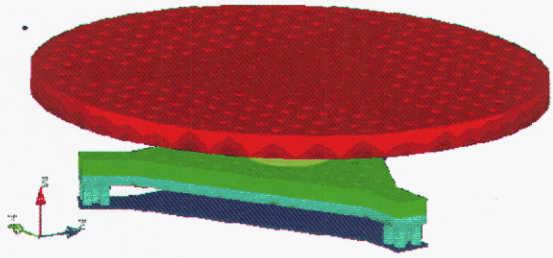

**Figure 41 500 µm MMpoly3 mirror generated in CoventorWare™.**

**Figure 42 FEA Model of 500 µm MMpoly3 Mirror with intrinsic stress displacements shown.**

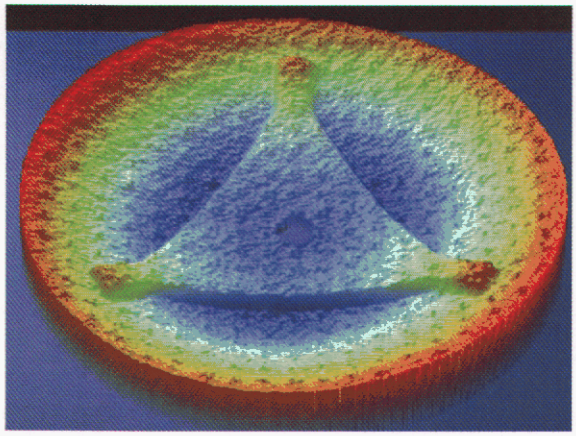

**Figure 43 3-D Interferogram of 500 µm MMpoly3 mirror.**

As another example of modeled mirror results, a more complex mirror is shown in Fig. 44. This mirror has an MMpoly3 and MMpoly4 mirror structure with an MMpoly4 surface, which is hollow between the two polysilicon layers. The assumption is made that the etch release holes allow for complete removal of the sacrificial oxide. The modeled deflection results are shown in Fig. 45, where a radius of curvature of +0.81 m was found compared to the interferometric results of +0.80 m shown in Fig. 46. These last two results help to validate the use of a modeling tool for a complex structure where straight-forward analytical solutions cannot be used.

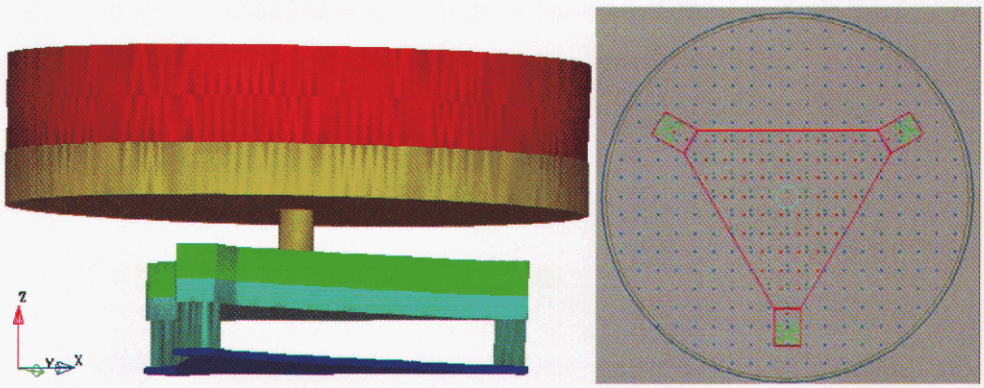


**Figure 44 500 µm MMpoly4 surface mirror. a) model of device b) 2-d layout of device.**

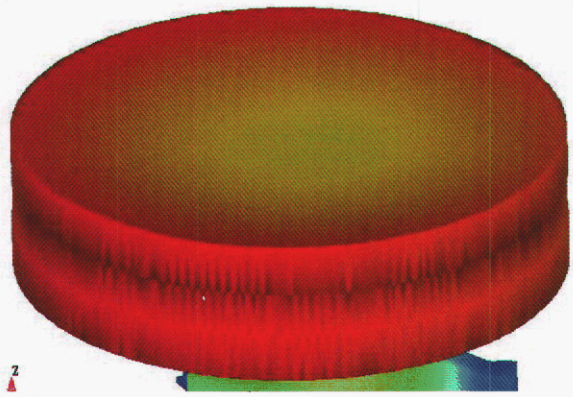

**Figure45. Modeled deflection results from 500 µm MMpoly4 surface mirror. Radius of curvature is +0.81 m.**

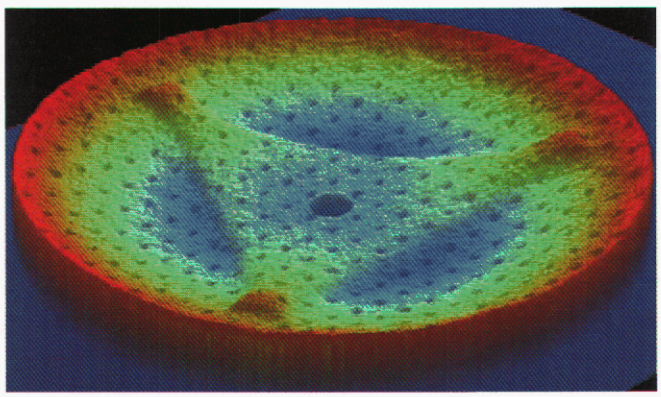

**Figure 46 3-D Interferogram of 500 µm MMpoly4 surface mirror. Radius of curvature found as +0.80 m.**

After the FEA code was validated with experimental results as discussed above, a more detailed study of the complex mirrors was completed. The detailed study included modeling the mechanical vertical stiffening members and including trapped oxide in the mirrors. Fig. 47 a) and b) depict a MMpoly4 mirror from the initial design layout with vertical stiffening members and trapped oxide, with more detail of the trapped oxide shown in Fig. 47 b). The figures are shown to demonstrate the complexity of these models and the fine mesh required when more internal structure is included in the device.

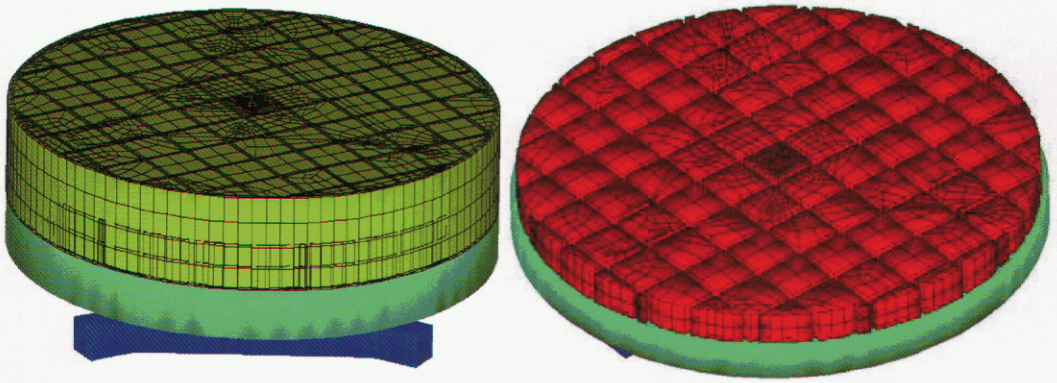

**Figure 47 a) 500 µm MMpoly4 mirror surface with mechanical reinforcements and trapped oxide. b) top surface is of trapped oxide mesh detail.**

The MMpoly4 mirror described above exhibits a radius of curvature of +0.9 m, as shown below in Fig. 48. The interferogram displays a significant amount of surface topography from the mechanical vertical stiffening members and trapped oxide. These unwanted optical features were analyzed and mitigated using parametric modeling methods to determine the best shape, location and quantity of mechanical vertical stiffening members and of trapped oxide arrangements.

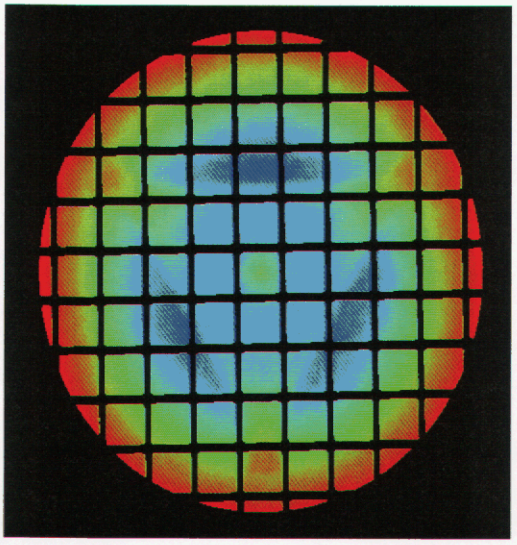

**Figure 48 Interferogram of 500 µm MMpoly4 mirror. The Radius of curvature is +0.9 m.**

### 5.2.2 Modeled Simulation Results

A summary of several modeled designs are shown in Fig. 49. The designs include first generation mirrors as labeled in Fig. 8, cantilever beams and second generation mirrors as labeled in Fig. 15. These results show the experimental, FEA modeled radius of curvature data, and the error between the two values shown in the last column. The error values vary due to not including all the topographical features in each design and the process variations, including not knowing the exact residual stresses, stress gradients, and layer thicknesses. However, the figure does not show the trends of behavior that are seen visually in the displacement results of the actual modeled mirror surfaces. Values such as the visual trends seen in the models and these shown in the following figure assisted in the design of the second generation of mirrors and provided evidence that the modeling can be used as a predictive modeling tool to create robust mirror designs.

| Design Description | Experimental (ROC) | Modeled (ROC) | Error |
|---|---|---|---|
| **1st Generation Mirror, C1** | 0.176 m | 0.222 m | 26.1% |
| **1st Generation Mirror, C2** | 0.17 m | 0.19 m | 11.8% |
| **1st Generation Mirror, C3** | 0.8 m | 0.81 m | 1.3% |
| **1st Generation Mirror, C4** | 0.267 m | 0.332 m | 24.3% |
| **1st Generation Mirror, C5** | 0.332 m | 0.322 m | 3.0% |
| **1st Generation Mirror, C6** | 0.45 m | 0.52 m | 15.6% |
| **1st Generation Mirror, C9** | 0.9 m | 1.04 m | 15.6% |
| **Cantilever Beams, P2** | 0.21 m | 0.23 m | 9.5% |
| **Cantilever Beams, P4** | 0.21 m | 0.2497 m | 15.9% |
| **2nd Generation Mirror, TH1C** | 0.12 m | 0.156 m | 30% |

**Figure 49 Summary of experimental and modeled results for several designs**

# 6 Actuator Design

One of the goals for the MEMS mirrors for adaptive optics applications is large stroke. Also, it is desirable for the mirrors to be able to tip and tilt as well as piston. Calculations indicate that a mirror that is able to piston, tip and tilt (PTT) more effectively removes wave front aberration than a piston only mirror. This is true despite the fact that PTT mirror requires 3 connections whereas piston only mirror needs one – fewer PTT mirrors are needed to remove the aberration to the same level. Figure 50 shows how well these two types of mirrors remove various types of wavefront distortion by plotting residual aberrations as a function of number of actuators (thus taking into account the 3:1 ratio of required actuator for PTT mirror vs. piston only):

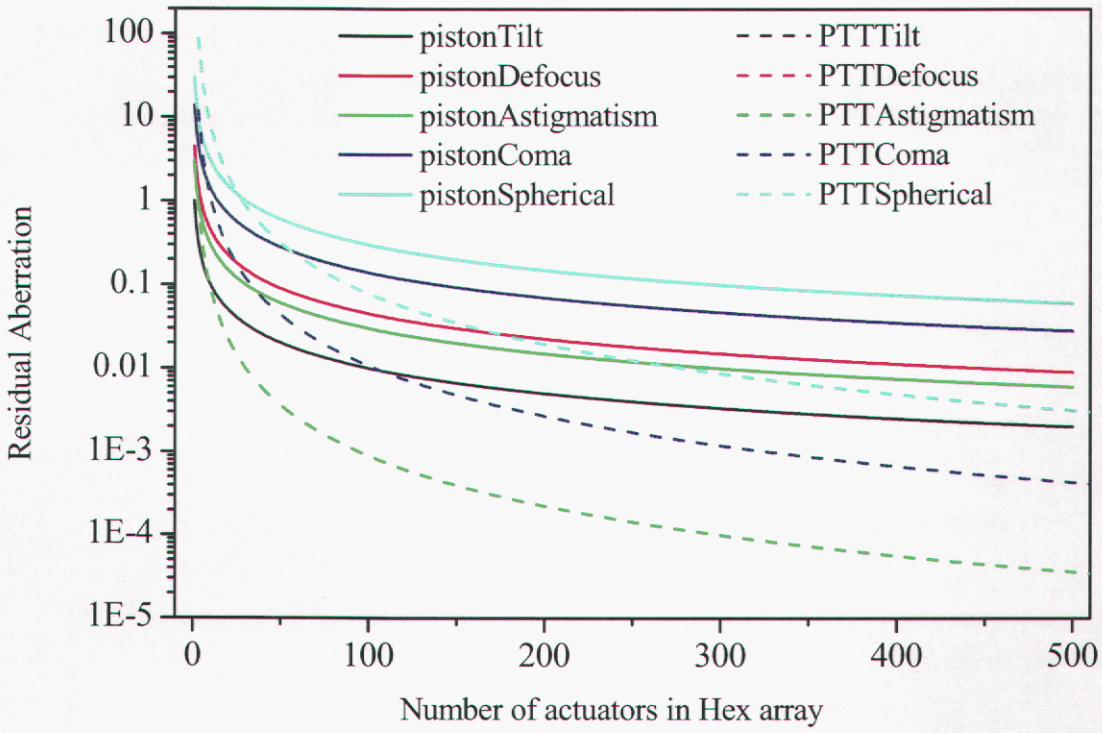


**Figure 50 Residual aberrations for several different types of wavefront distortion after removal by piston only (solid lines) and PTT (dashed lines) mirrors as a function of required actuators.**

## 6.1 Actuator Types

Most MEMS mirrors employ electrostatic actuation. We dismissed thermal actuators despite the potential for large strokes and high force principally because of their large power dissipation. When one considers that optical aberrations in the atmosphere and indeed in optical systems are induced primarily by thermal gradients it is easy to dismiss large arrays of thermally actuated mirrors as a serious approach. Though it may be premature to dismiss thermally actuated MEMS mirrors entirely, we focused on the design trades associated with increasing the stroke of electrostatic actuators.

Consider a simple parallel plate electrostatic actuator comprised of a movable upper electrode supported by a spring of total linear spring constant, k, and a fixed lower electrode attached to

the substrate. When a voltage is applied across the electrodes the attractive force ($F$) between the plates is found by integrating the charge difference across the overlapping electrode areas. For typical MEMS mirrors actuator geometries, fringing fields and deformation of the mirror plates can be neglected. Integrating the charge yields the electrostatic force,

$$F = \frac{A\varepsilon_0 V^2}{2g^2} \tag{6.1}$$

where $A$ is the overlapping electrode area, $\varepsilon_0$ is the dielectric constant of air $8.854\times10^{-12}$ F/m, $V$ is the voltage across the electrodes, and g is the gap between the electrodes. Because the upper electrode moves it is represented by the as-fabricated height minus the deflection of the plate, $g=h-d$.

$$F = \frac{A\varepsilon_0 V^2}{2(h-d)^2} \tag{6.2}$$

For small deflections the counter force applied by the linear spring flexures is $F=kd$, from Hooke's Law. The force balance equation for the system is,

$$kd = \frac{A\varepsilon_0 V^2}{2(h-d)^2} \tag{6.3}$$

Note that this simple model neglects a common phenomenon of electrostatic devices. As the deflection of the upper electrode approaches about 1/3 the total gap distance, the electrostatic force is increasing much more rapidly than the linear restoring force of the spring flexures. As a result the system becomes unstable, and the upper electrode snaps down to the fully deflected position [55]. If the upper and lower electrodes come into contact with each other they can be permanently stuck together, destroying the device. This characteristic snap-through instability behavior typically limits controllable deflection to less than 1/3 the as-fabricated gap.
But having noted that snap-down is a real concern we will ignore it for now and look only at the impact of increased stroke or deflection, $d$. First it is obvious that increasing the gap is required and the maximum voltage required for full deflection must increase as linear function of the gap. In general it is both practical and desirable not to arbitrarily limit operating voltages in electrostatic devices because higher control voltages allow the stiffest, fastest actuator structures in a given area. Control voltages up to 300V are reasonable for high voltage CMOS technologies [56]. Without delving into the details of actuator stiffness and electrode area this control voltage range typically limits practical electrostatic actuator deflection (or MEMS mirrors) to less than 10 microns. In addition large gaps require deposition, patterning, and release etching of thick sacrificial layers, which are not available in the SUMMiT process. This problem can be avoided by employing stressed beams to establish an increased actuator gap in a self-assembly process. While their approach shows promise, one inherent limitation is that reliance on the bimorph lifting structure will impose a temperature sensitivity that may be undesirable for space applications.

Rather than simply increasing the electrostatic actuator gap it is better to employ reasonable gaps and mechanically convert the downward gap closing actuation into an upward motion (away from the substrate). This is compatible with the release layer thicknesses available in SUMMiT. In the following sections three types of high-stroke electrostatic actuators comprised of levers, buckled beams and zipping structures are briefly explored and specific designs under development at Sandia detailed.

**a. Levers**: Amplify and invert vertical deflection

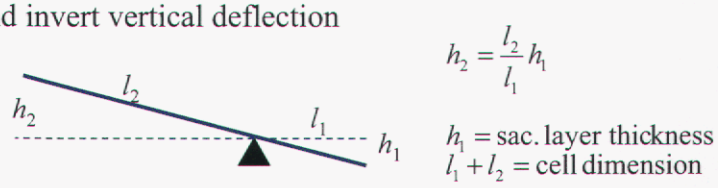


**b. Buckled Beams**: Translate lateral force into amplified vertical deflection

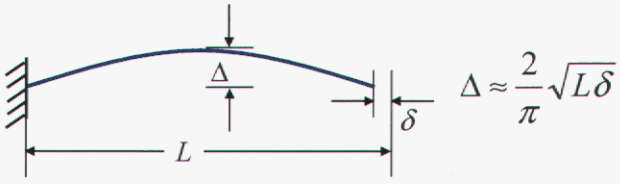


**c. Zippers**: Amplify vertical deflection (variation of lever)

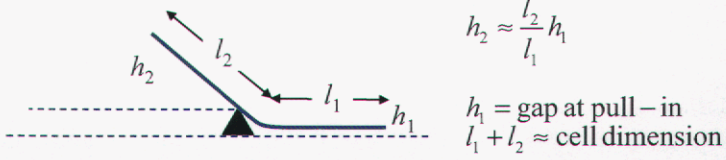


**Figure51. Mechanical methods for stroke amplification**

### 6.1.1 Levers

As depicted in Figure 51a, a simple lever can be used to invert and amplify the stroke of a gap closing actuator. In theory very large deflections are possible, but before one gets carried away it must be noted that practical applications require that the lever and actuator length ($l_1$ + $l_2$) must be less than or equal to the mirror cell size. The gap, $h_1$, will be determined by the sacrificial layer or layers available in the microfabrication process. For the SUMMiT process $h_1$ is either 2 μm (sacox1) or 6.5 μm (sacox1 + MMpoly1&2 + sacox3). Practical dimensions of $l_1$ are a function of the gap selected, actuator width, spring stiffness and the force required to move the mirror plate. A plan (a) and cross sectional (b) view of a lever actuator layout is shown in Figure 52. In Figure 52 (b) pivot, lever arm and the actuation electrode are indicated as well. This particular actuator was used to elevate a hexagonal mirror in three corners in an array of mirrors that will be discussed in subsequent sections.

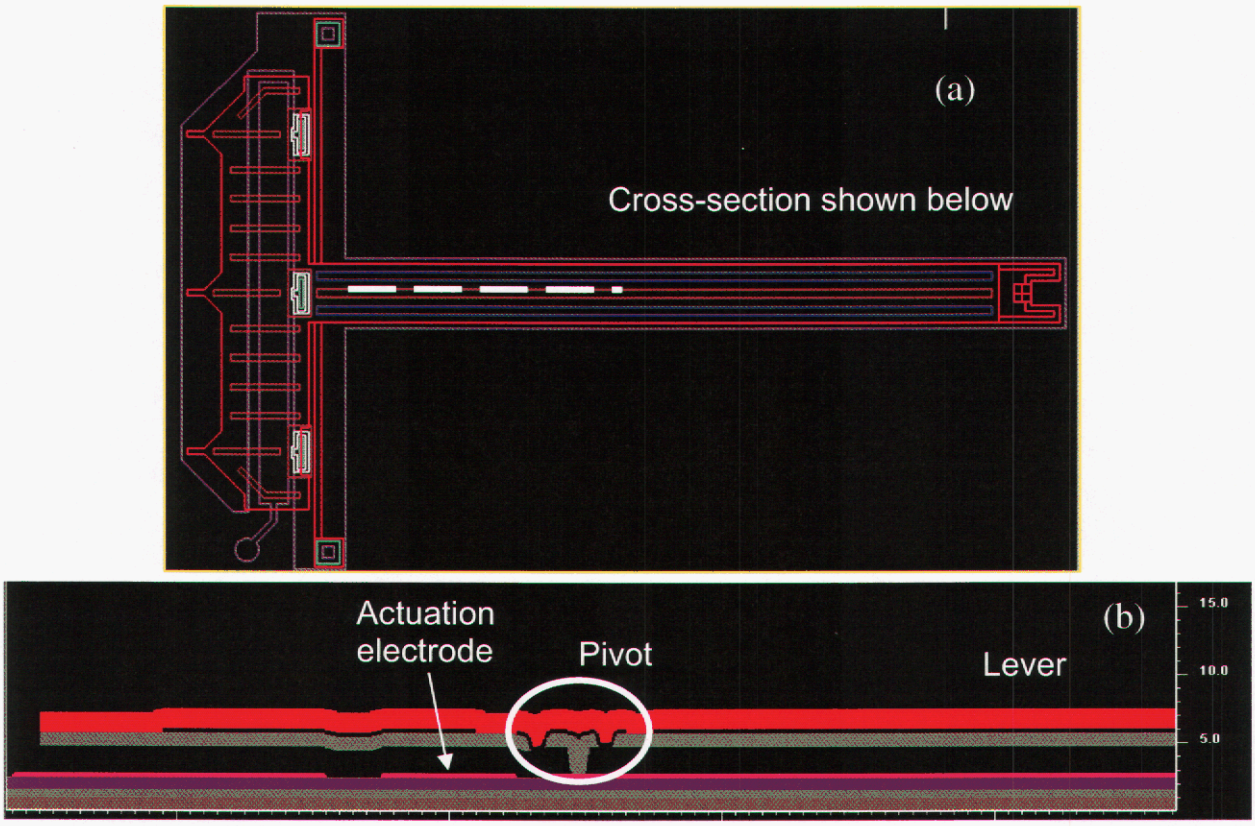


**Figure 52 (a) plan view of a lever actuator with a line indicating where the cross sectional view shown in (b) is taken**

Predicted deflection of the lever actuator shown in Figure 52 is 13.7 μm as dictated by equations in Figure 51a. These are approximate due to the fact that initially the lever will rotate about the torsion spring, until the actuator plate contacts the underlying pivots, then the lever will rotate about the pivots. It also should be noted that this design of the actuator is somewhat conservative in that it uses only MMpoly1 and MMpoly2 for the actuator, leaving MMpoly3 and MMpoly4 for increased stiffness mirror. Consequently the expected stroke is compromised. Other designs explore actuators which utilize MMpoly2 and MMpoly3 and thus have a higher expected stroke. For example lever actuator shown in Figure 53 has the expected stroke of 27.5 μm. This however leaves only MMpoly4 for the mirror structure, potentially compromising mirror figure. It would be most advantageous to control stress and stress gradient in MMpoly4 in such a way that it would be unnecessary to use MMpoly3 to balance out MMpoly4, which would allow for the use of MMpoly3 in the actuator structure, while assuring a good mirror figure utilizing only MMpoly4 for the mirror. We are currently investigating schemes that would allow this scenario.

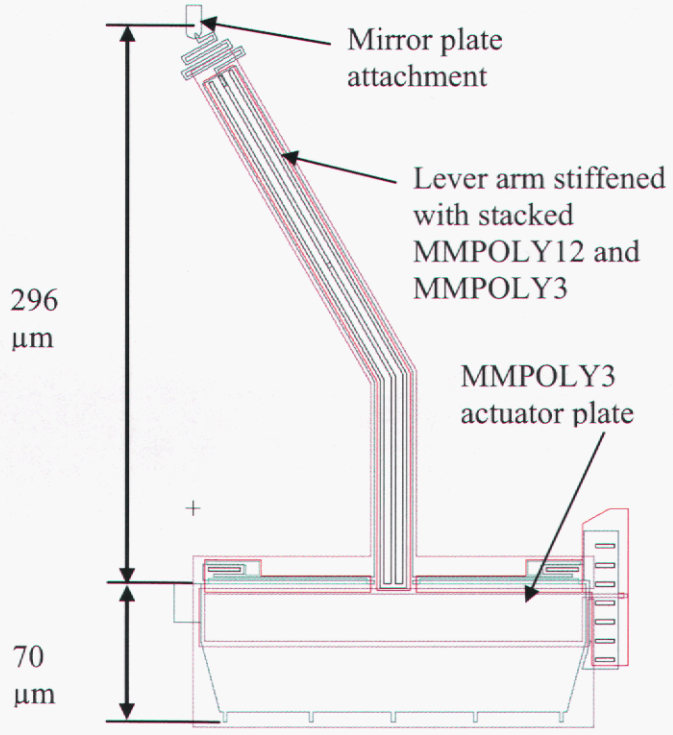


**Figure 53 Lever actuator utilizing MMpoly2 and MMpoly3 thus achieving a greater stroke**

Actuators shown in Figure 52 and Figure 53 are arranged under a hex mirror in a manner shown in Figure 54a and 54b respectively. There are three attachment points, separated by 120° allowing tip/tilt motion when the three actuators are actuated to uneven stroke and piston motion when they are actuated simultaneously to the same deflection.

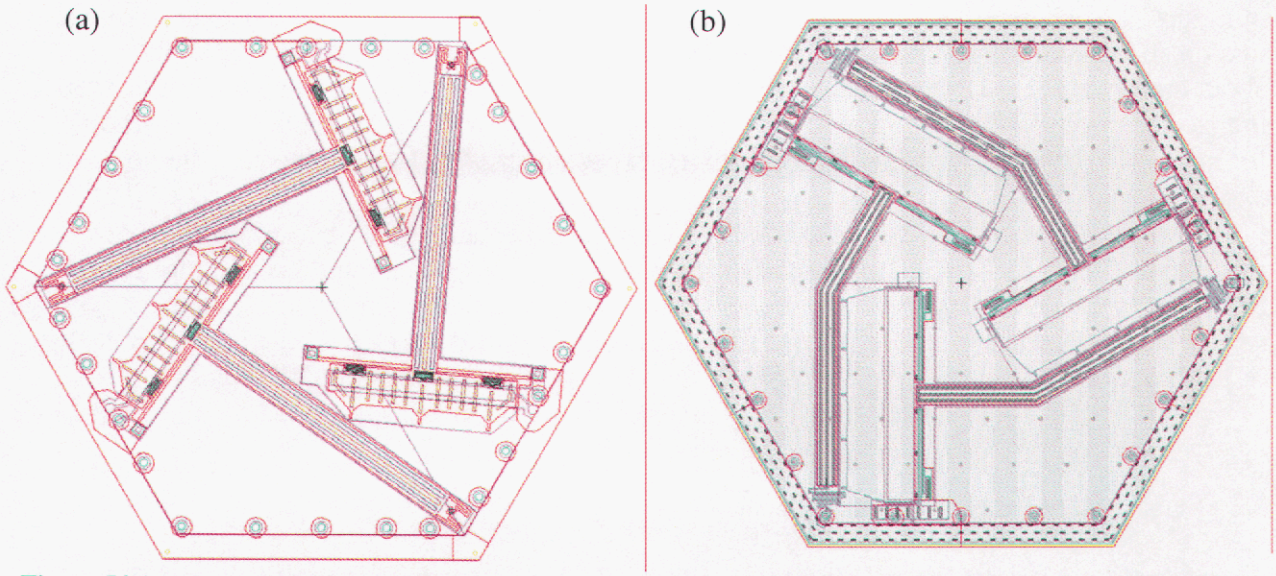


**Figure 54 Arrangement of lever actuators underneath a hex mirror using actuators shown in (a) Figure 52 (b) Figure 53**

We have measured displacement of a mirror such as the one shown in Figure 54a as a function of bias on individual actuators separately and together, thus implementing tip/tilt and piston functions. Figure 55 shows the behavior of the mirror surface as function of bias applied on the individual actuators together and separately:

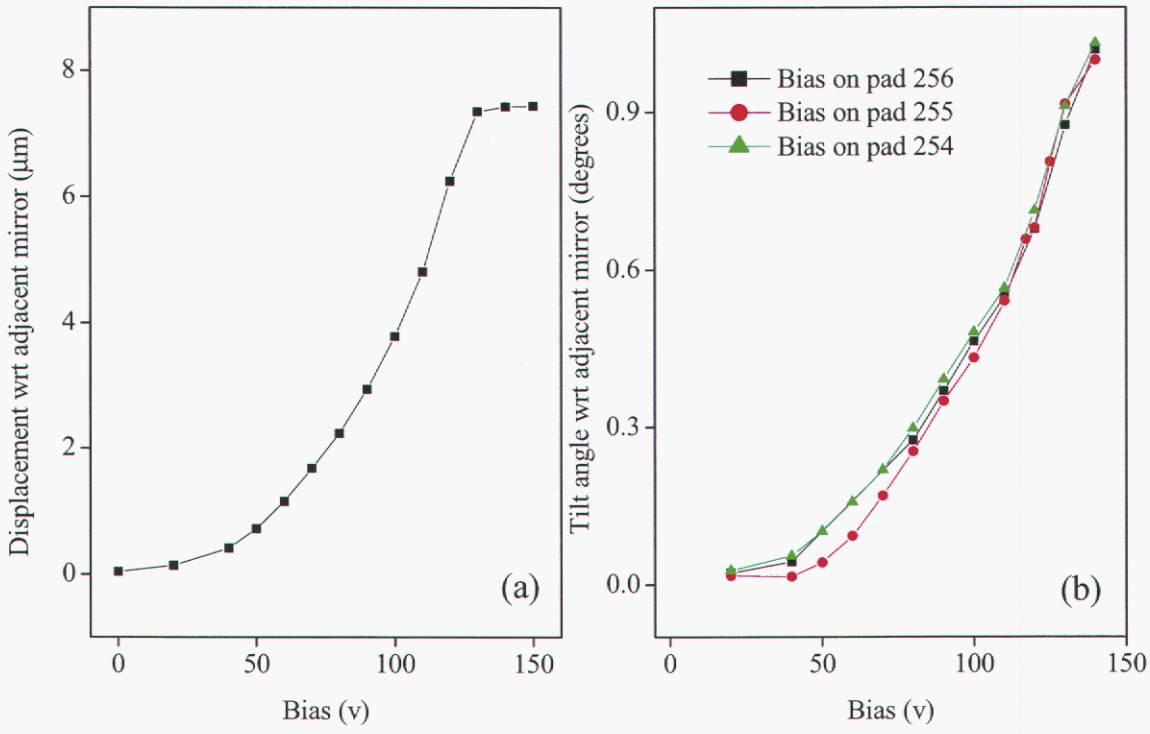


**Figure 55 a) Piston motion of the MEMS mirror when actuators are biased together at a x-axis bias b) Tilt/tip of the MEMS mirror when an x-axis bias is applied at a single actuator, while others are grounded**

Shown in Figure 56 is the interferometric 3-D representation of a MEMS mirror tipped, tilted and pistoned to an arbitrary position. Bias on the actuators is 90, 120 and 140 V, which represent 33%, 66% and 100 % of available deflection on each actuator respectively.

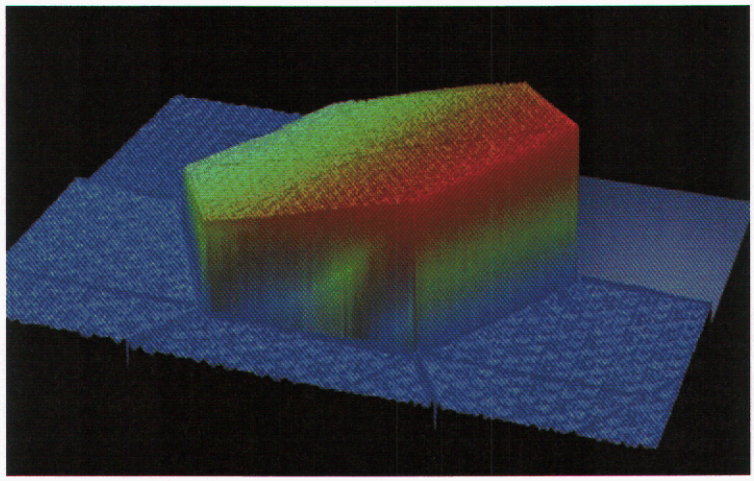

**Figure 56 3-D interferometric image of an actuated mirror at an arbitrary position**

## 6.2 Buckled Beams

Beam buckling can also be used to achieve large deflections from small actuator strokes as shown in Figure 51b. For example an actuator stroke, $\delta$ of only 2 μm can produce an upward vertical deflection, $\Delta$ of ~14 μm for a 250 μm long beam. Beam buckling deflection amplification has been exploited extensively by MEMS designers for other structures but has not been used for MEMS mirrors. The principal reason for this is that beam buckling requires high forces that are difficult to obtain electrostatically. Also note that although the center of the buckled beam is ideally parallel to the substrate at all times, thus proscribing a pure piston motion for an attached mirror, even slight fabrication variations could cause undesirable tilt. Therefore three actuator piston-tip-tilt designs are most feasible. Conceivably very large (~50 μm) strokes are possible with buckled beam actuators if the required electrostatic forces can be generated. Again for practical MEMS mirrors the maximum length ($L$) of the buckled beam is about the same as the mirror cell size. We did not pursue this type of actuator design for the MEMS mirrors, due to difficulty in generating sufficiently large forces in an area defined by the mirror surface (this is a necessity in a tightly packed array).

### 6.2.1 Zipper Actuators

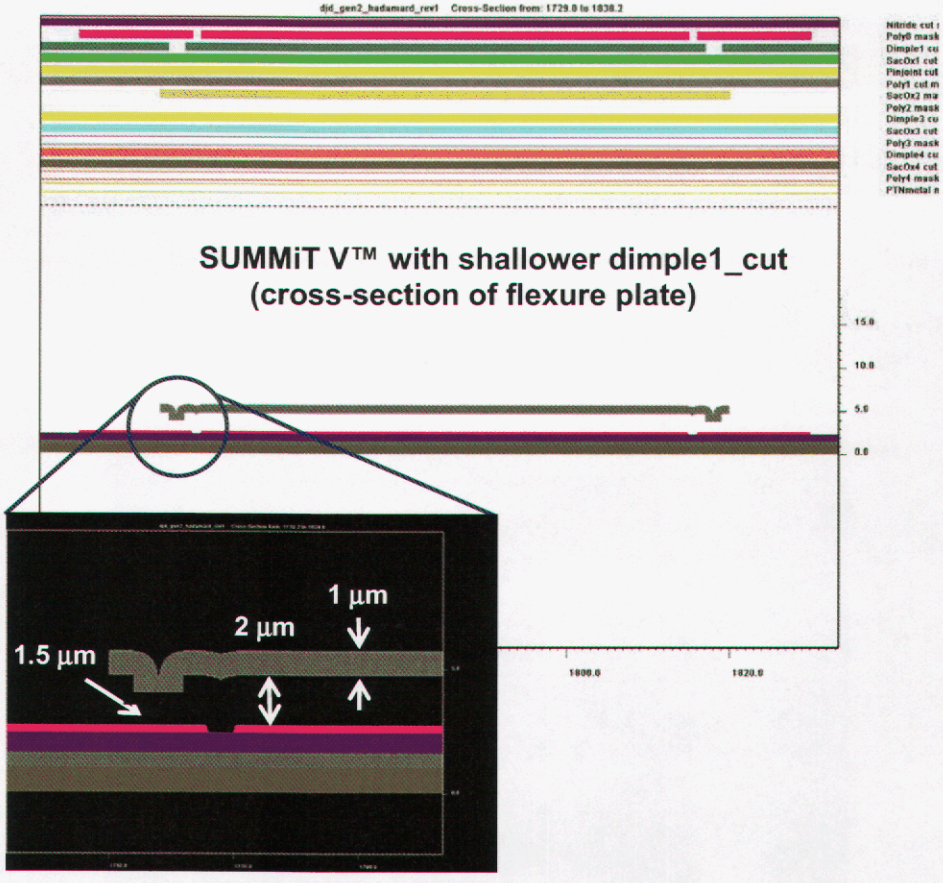


**Figure 57 Cross section of the zipper actuator with the inset showing detail of the flexural plate**

Zipper actuators represent a variation of the basic lever where the zipper exploits the increased electrostatic force available with a small actuation gap to bend the actuator plate and thereby increase the maximum deflection of the lever tip. One of the key concerns with zipper actuators is reliability. Zipping structures require comparatively large contact area between the zipper structure and mechanical stops, and mechanically stress the zipper material severely, both of which may limit zipper actuator reliability. Despite these unknowns experimental zipper actuators have exhibited very promising strokes and are currently being used for MEMS mirrors. Figure 57 shows a solid model of a zipper actuator:

Various variations of zipper designs have been explored. One of the parameters varied was the depth of the dimple1_cut which determines the distance that the flexural plate displaces down as it zips along its length. In Figure 58 which shows a cross sectional view of a zipper design, that parameter is 1.5 μm and is indicated in the inset. Designs where the gap varied from 0.5 μm to 3 μm were fabricated and evaluated. Shorter dimples provided more stroke at lower voltages but required extra care to avoid electrical shorts. Another design consideration involved the material on which the flexural plate landed. Inset in Figure 58 shows that the polysilicon zipper lands on polysilicon landing pad (MMpoly0 indicated with a pink line). This is necessary to prevent charging, as in the case of landing on SiN, which then leads to hysterisis in the actuation. Figure 59 shows measured deflection of the zipper tip as a function of applied voltage for two different width zippers. While total displacement as large as 12 μm was observed, only the portion after the snap down is usable. This large usable displacement (i.e. displacement after snap down) of ~6 μm is observed for applied voltages near 100 V and is shown in Figure 59.

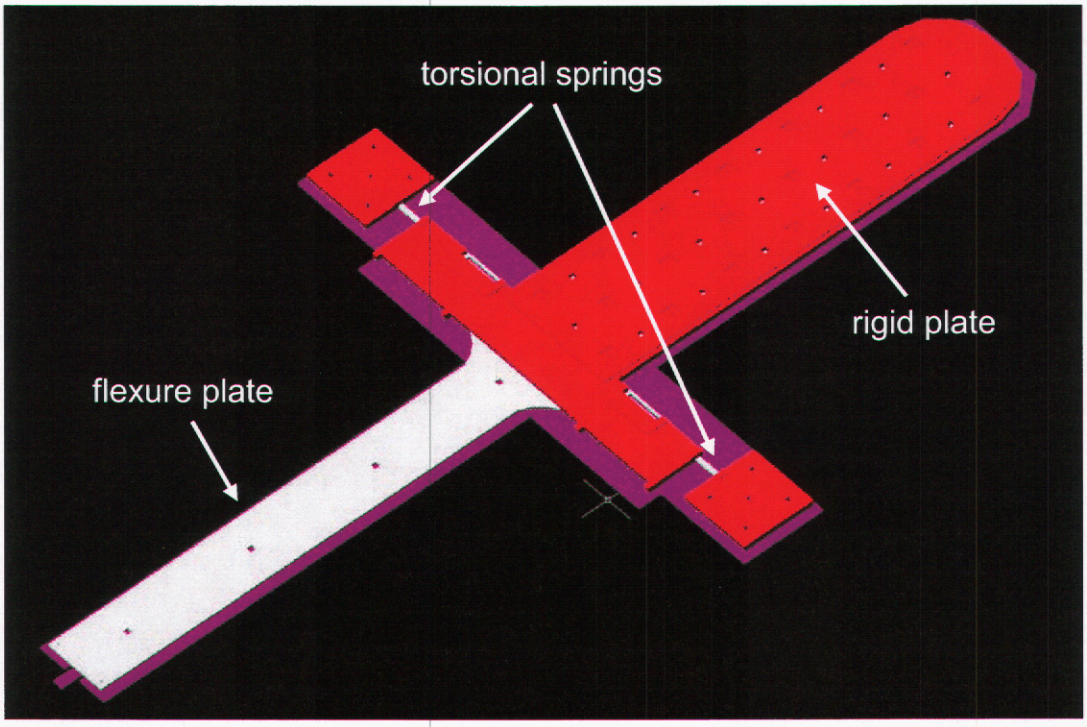


**Figure 58 Solid model of a basic zipper design**

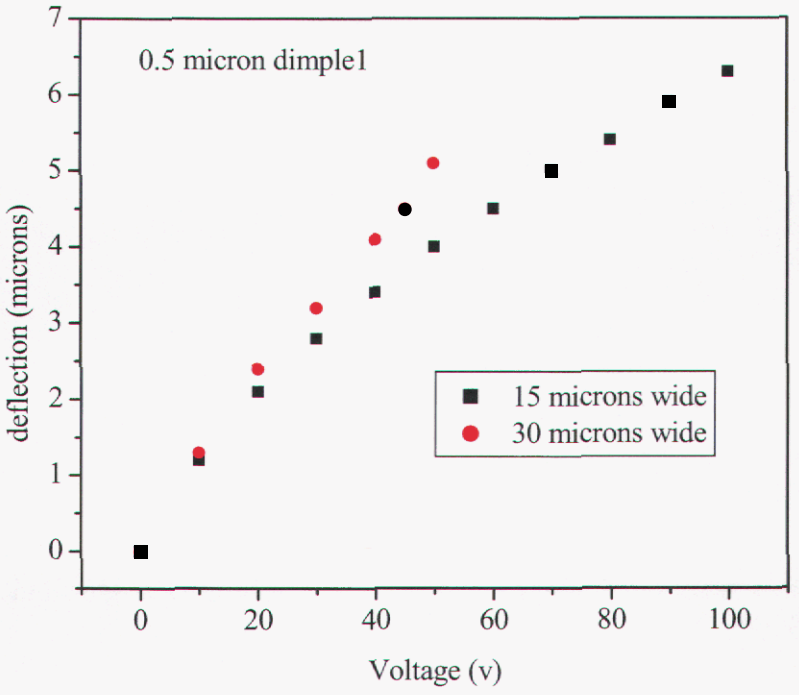


**Figure 59 Deflection as a function of voltage for a zipper actuator with two different widths**

Shown in Figure 60 is the arrangement of the zipper actuators underneath the hexagonal mirror for an edge pivot (a) or center pivot (b). In either case, mirror can be deflected at points 120° apart by actuation of any one or combination of zippers thus implementing a tip or tilt. Actuation of all three zippers simultaneously by same amount results in piston motion.

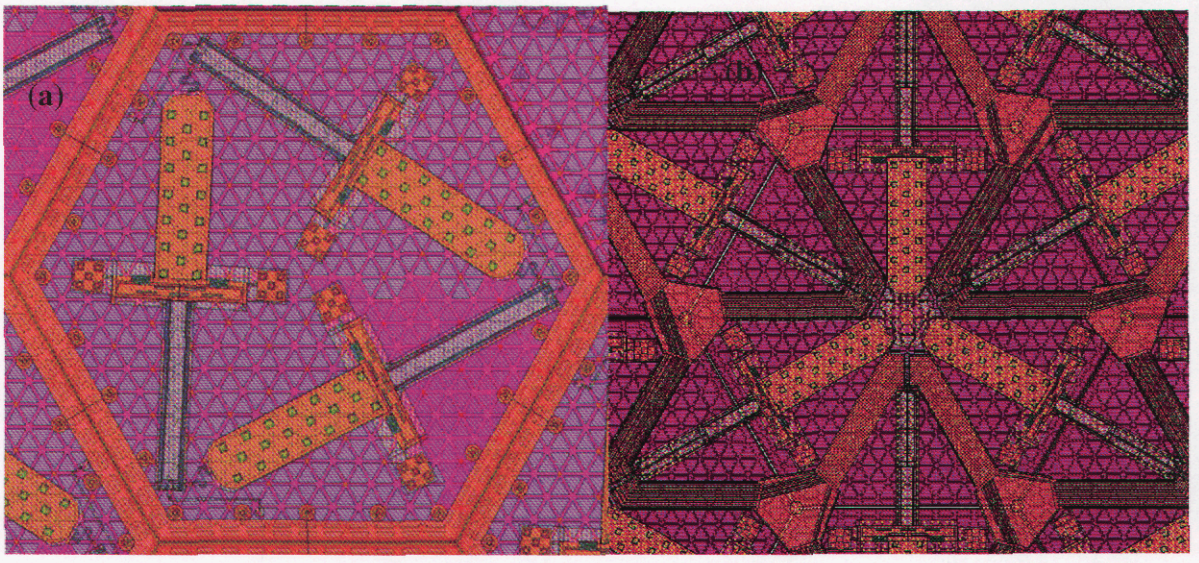


**Figure 60 Arrangements of zipper actuators underneath a hexagonal mirror (a) edge pivot (b) center pivot**

# 7 Arrays

Several types of arrays have been designed and fabricated. In general they are hexagonal arrays of hexagonal mirrors with three actuators under each mirror. Final size of the array is limited by the pin out and package availability. Under the guise of another activity we have developed and exercised back-end-of-line (BEOL) processes for the mature SUMMiT polysilicon micromachining process that include metallization of mirrors and packaging. Using automated die attach and automated wire bonding packaged micromirror parts of up to 200 actuators have been successfully delivered on other programs. We have leveraged these developments for demonstration of AO MEMS mirror subsystem that includes metallized, packaged arrays and drive electronics and software.

## 7.1 Array types

The primary design (AO255) comprises an array of 91 hexagonal piston-tip-tilt 500 µm size elements on a hexagonal grid as shown in Figure 61a. The 6 corner elements are inactive leaving an active circular aperture of ~3.9 mm diameter with 85 active mirror elements (255 actuators). The layout of a single element is shown in Figure 61b. The mirrors employ an MMpoly4 plate reinforced with and MMpoly3 honeycomb structure. As mentioned previously, the reason that a full plate of MMpoly3 is not used for reinforcement is that previous work has shown that excess MMpoly3 pattern density causes problems with the chemical mechanical polishing steps critical to the SUMMiT process. The reinforced mirror plate is supported by 3 lever actuators of the type shown in Figure 52.

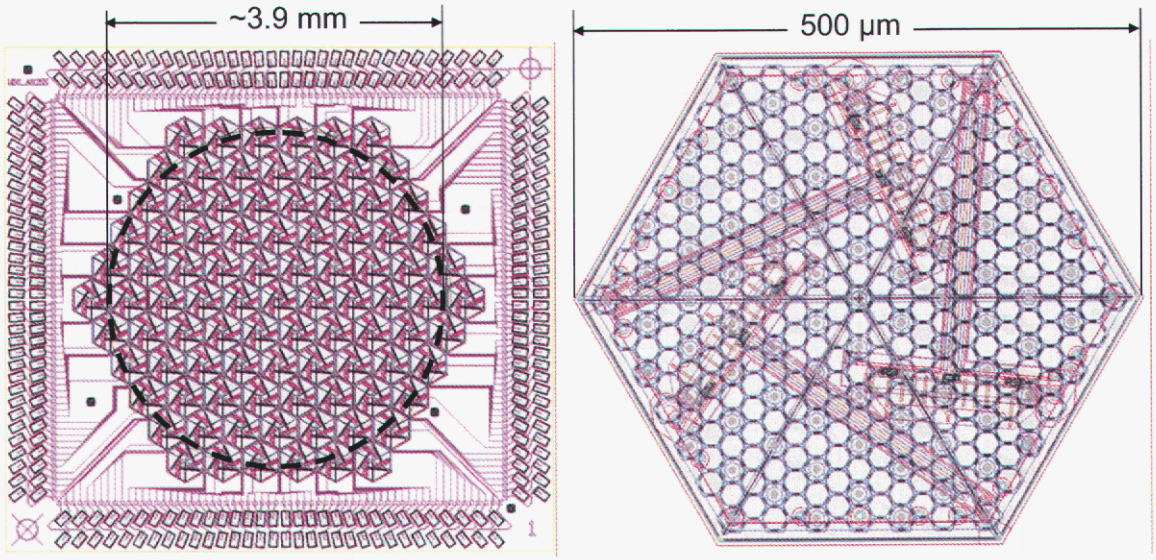


**Figure 61 a) Layout of a 91 element array b) view of a single mirror**

In addition to mask layers for BEOL metallization, the AO255 design includes self shielding provisions in the array area to allow a wide variety of post-fabrication mirror coatings. Alignment marks for simple shadow masks to protect the chip periphery are included in the upper right and lower left corners of the die.
The principal risks for the AO255 design are the novel lever actuators (although the early data indicates acceptable performance) and the 256 pad pinout. While packaging of 208 pad chips of this size has been remarkably successful, the pad pitch and long wire bonds required for the 256 pin package pushes the limits of the automated packaging processes.
Shown in Figure 62 is a photograph of a fabricated AO255 array before packaging:

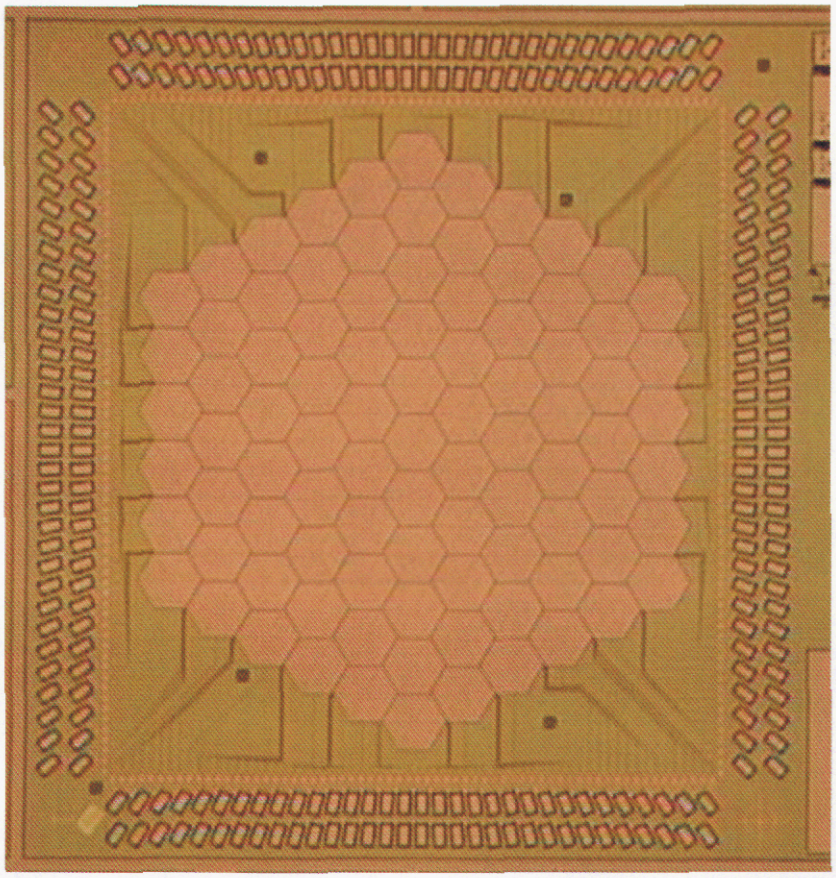

**Figure 62 Fabricated AO255 array (91 element hex) before packaging**

Four different large stroke MEMS mirror array designs were pursued on a secondary design (AO208). All of these designs employ the 208 pad frame developed and successfully demonstrated for another project. Each array consists of 61 hexagonal piston-tip-tilt elements that are nominally 500 μm side-to-side (rather than corner-to-corner as in AO255). These larger mirror elements offer the potential for increased stroke. A layout view of the AO208 designs is shown in Figure 62, with annotations denoting the actuation mechanism employed and estimated stroke. The circular aperture for all designs is 3.78 mm diameter.
Comparison of these designs to the AO255 design illustrates the trade of stroke and element size. The BH_3 design (upper right corner of Figure 63) employs actuator dimensions (l1 and h1) that are identical to the AO255 design, but a longer lever arm (l2) increases the estimated maximum stroke by about 25%. The BH_1 design (upper left corner of Figure 63) trades mirror

reinforcement for an increased actuator gap (h1) resulting in a roughly doubled estimated stroke. The downside of this trade is that acceptable mirror flatness using the BEOL metallization developed to date is unlikely. Thus the BH_1 arrays will require post release metallization. Both zipper actuator MEMS mirror designs on AO208 are expected to achieve about 12 μm stroke. The mirror plates in both designs are fully reinforced with MMpoly3 honeycomb structures but the method of attachment to the MMpoly4 layer differs.

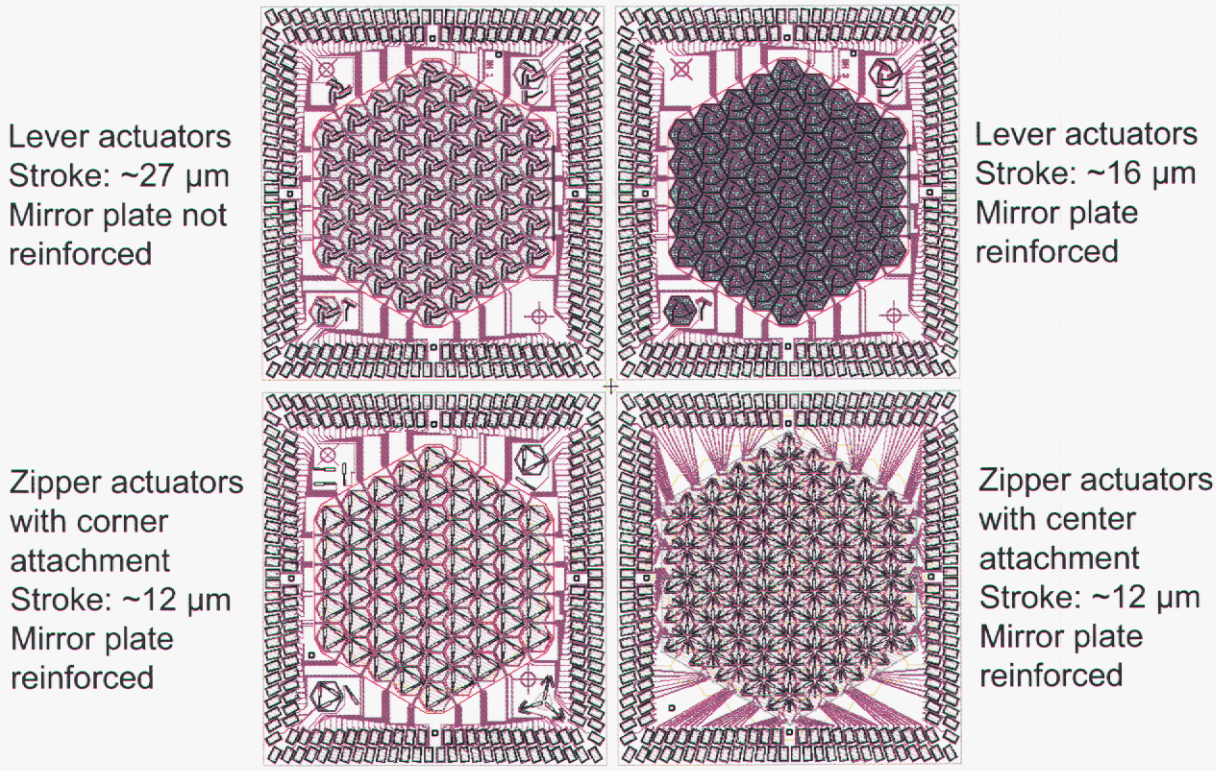


**Figure 63 Layout of the secondary AO MEMS mirror array designs (AO208)**

## 7.2 Drive Electronics and Board Design

Addressing 256 or 208 pads independently is not trivial. In order to facilitates the usage of the arrays in a system we have designed and fabricated drive boards which take advantage of commercially available components. We have relied heavily on our previous experience in fabricating a drive electronics system for another project where 100 mirrors with 2 interconnects each were driven independently to several discrete tilts. In this case, our drive electronics are complicated by the fact that AO mirrors require analog control of the position.
Figure 64 shows a photograph of a board that was built to independently control mirrors packaged in a 208 pin PGA.

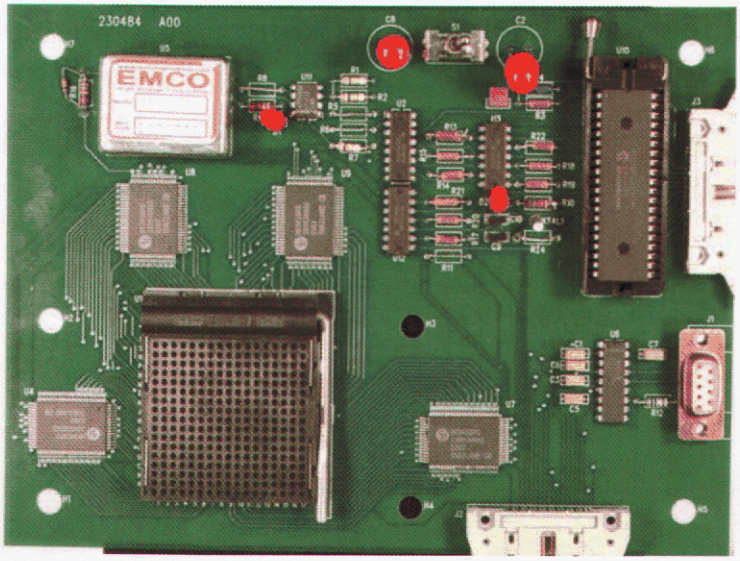


**Figure 64 Drive board for a 208 pin PGA packaged MEMS mirror arrays populated with drive electronics**

Mirror positions are programmed in a computer and then down loaded into the drive electronics on the board. Pre-determined mirror positions can also be programmed into a programmable integrated circuit (PIC) and plugged into the board directly, where DIP switch positions determine which pattern the mirrors will be programmed into.
The schematic for a board for driving 256 pin PGA AO MEMS is shown below in Figure 65:

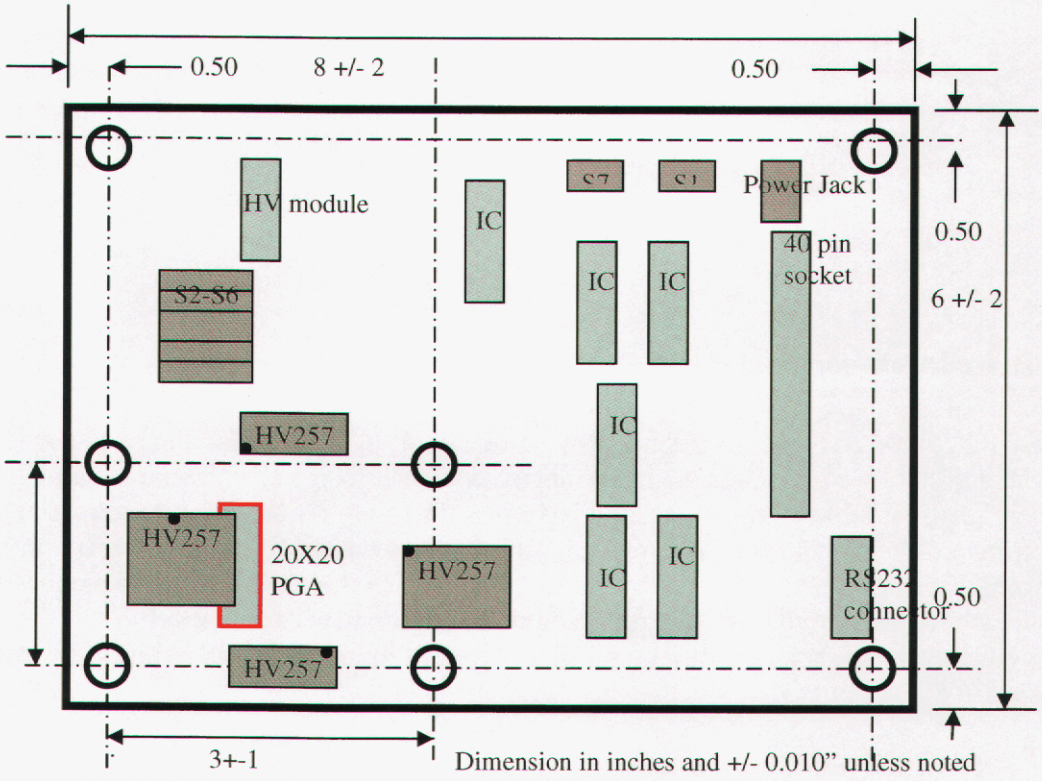


**Figure 65 Schematic layout of a board for driving AO MEMS mirror array packaged in a 256 pin PGA**

# 8 Future Work

As presented in the preceding sections, stress gradients and residual stresses have been measured for accurate modeling of micro-mirrors. Through this modeling study, relevant structural parameters have been identified, which are necessary to optimize SUMMiT V™ MEMS mirrors for optical applications. Methods for mitigating surface topography, print-through effects, and RMS roughness have been detailed. Multiple mirror structures were designed, fabricated, characterized, and modeling efforts have shown what structural parameters are important for gaining optically flat mirror designs. Through these efforts, 500 μm mirrors have been demonstrated with surface roughness close to λ/20 and radius of curvature on the order of 1 m.

Also discussed is the finite element modeling study, which creates a coupled modeling and design technique that demonstrates a predictive design tool. This finite element modeling study provides a potentially inexpensive alternative to empirical designing when taking into account the total time and cost of fabrication. Modeling of MEMS devices is beneficial to the designer, given that foundry turnaround times are on the order of several months. Pre-fabrication analysis allows the designer to determine how his device or system will behave under many different cases without ever having to build a structure. In order for the modeling effort to be productive, it must begin with a good understanding of the fabrication parameters and any process variations or limitations. These parameters, which are essential to the success of understanding the design include, but are not limited to, residual stresses, stress gradients, layer thicknesses, permittivity of films, pattern density, and wafer curvature. It is important to have bounds for these parameters for initial modeling, although exact values are needed after fabrication of the devices in order to validate results.

One aspect of mirror figure not addressed by this work is metallization. This is an important area of study as the final reflective layer can be a major contributor to mirror deformation due to reflective material stress and stress gradient as well as thermally induced deformation due to coefficient of thermal expansion mismatch between the reflective material and the polysilicon structural layers. There are multiple ongoing efforts aimed at characterizing and improving stress characteristics of various reflective surfaces, such as metals or dielectric layers. Another important ramification of the reflective surface is the ability of the mirror to handle high optical powers. Due to small thermal mass, MEMS mirrors in general do not handle large optical powers well, because even moderate amount of absorption in the polysilicon layers results in significant rise in temperature which can deform or even catastrophically damage the mirror surface. Thus high reflectivity coating is essential to prevent absorption and thus heating in the mirror. While this is not a large concern for imaging applications such as ultra lightweight telescope, other adaptive optic applications such atmospheric correction of high power lasers maybe limited by this issue.

Further work on optimization of the actuator schemes and more complete characterization of their uniformity across the array and sample to sample are required. This is needed as an input to drive schemes and achieving sufficient uniformity will significantly simplify drive electronics. For the scope of this program, we have limited ourselves to array sizes sufficiently small so that they can be packaged in conventional packages and using surface trace technology. A very large obstacle that is common to many applications of optical MEMS is the lack of a parallel interconnect scheme that would facilitate fabrication of large arrays consisting of many mirrors. For an NxN mirror array, surface trace technology requires mxN2 interconnects where m is the number of interconnects per mirror (thus for a piston only mirror m=1, whereas for a piston/tip/tilt mirror m=3). A parallel interconnect would reduce the number of interconnects to

2xmxN for a same size mirror array. Largest package demonstrated to date is a 1000 pin PGA which in the case of surface interconnects implies a modest 32x32 mirror array for piston only mirrors. With a parallel interconnect, a 500x500 mirror array of the same type could be packaged in a standard package. Because of the high temperature cycles inherent in SUMMiT process, it is not in general compatible with integration with CMOS and thus alternative solutions are being pursued. These include various substrate via approaches combined with bump bonding to a separate CMOS chip, as well as customized electronics that can withstand high temperatures inherent in SUMMiT process.

Thus while a substantial progress has been made under the auspices of this program and we are now poised to demonstrate an MEMS mirror based AO subsystem in a larger optical system many challenges still remain.

## References


1 J. Comtois, A. Michalicek, W. Cowan, J. Butler; "Surface-micromachined polysilicon MOEMS for adaptive optics;" Sensors and Actuators, Vol. 78, pp. 54-62, 1999.

2 Claire Max, UC Santa Cruz, CfAO, "Adaptive Optics and its Applications, Lecture 1, March 26, 2002."

3 N.D. Masters, M.P. de Boer, B.D. Jensen, M.S. Baker, D. Koester; "Side-by-side comparison of passive MEMS residual strain test structures under residual compression;" *Mechanical Properties of Structural Films, STP No. 1413*, S. B. Brown and C. L. Muhlstein, Eds., American Society for Testing and Materials, West Conshohocken, PA, 2001.

4 D.L. Hetherington, J.J. Sniegowski; "Improved Polysilicon Surface-micromachined Micromirror Devices using Chemical-mechanical Polishing;" Presented at the International Symposium on Optical Science, Engineering, and Instrumentation, SPIE's 43rd Annual Meeting, San Diego, CA, July 22, 1998.

5. M.A. Michalicek, N. Clark, J.H. Comtois, H.K. Schriner; "Design and simulation of advanced surface micromachined micromirror devices for telescope adaptive optics applications;" *Proc. SPIE*, Vol. **3353**, pp. 805-815, 1998.

6. E.J. Garcia; "Pivoting micromirror designs for large orientation angles;" *Proc. SPIE*, Vol. **4178**, pp. 126-136, 2000.

7. F.R. Gass, J. Dohner, O.B. Spahn, E. Garcia, G. Grossetete; "An Investigation into the Response of a Micro Electro Mechanical Compound Pivot Mirror Using Finite Element Modeling;" *SPIE Photonics West: Integrated Optoelectronics Devices (Jan '03).*

8. O.B. Spahn, E.J. Garcia, V. Esch, G. Grossetete, F. Bitsie, S. Mani, J. Jakubczak; "Optical performance of pivoting micromirrors;" *Proc. SPIE*, Vol. **4561**, pp. 283-292, 2001.

9. W.D. Cowan, V.M. Bright, M.K. Lee, J.H. Comtois, M.A. Michalicek; "Design and testing of polysilicon surface-micromachined piston micromirror arrays;" *Proc. SPIE*, Vol. **3292**, pp. 60-70, 1998.

10. F.R. Gass, D.J. Dagel, D. Adams, G. Grossetete, O.B. Spahn, S. Kemme, S. Mani, K. Malloy; "Stress and Curvature in MEMS Mirrors;" *SPIE Photonics West: MOEMS and Miniaturized Systems III,* 2003.

11. S. Kemme, O.B. Spahn, F. Gass, D. Dagel, G. Grossetete; "Optical System Properties of a Reconfigurable MEMS Interconnect;" *SPIE Photonics West: MOEMS and Miniaturized Systems III,* 2003

12. D. Dagel, O.B. Spahn, J. Allen, S. Kemme, G. Grossetete, F. Gass; "Out-of-plane, rotary micromirrors for reconfigurable photonic applications;" *SPIE Photonics West: MOEMS and Miniaturized Systems III,* 2003.

13. M.A. Michalicek, J.H. Comtois, C.C. Barron; "Design and characterization of next-generation micromirrors fabricated in a four-level, planarized surface-micromachined polycrystalline silicon process;" *Innovative Systems in Silicon Conference*, pp. 144-154, 1996.

14. M.E. Warren, O.B. Spahn, W.C. Sweatt, R.J. Shul, J.R. Wendt, G.A. Vawter, T.W. Krygoski, D. Reyes, S.M. Rodgers, J.J. Sniegowski; "Integration of optoelectronics and MEMS by free-space micro-optics;" Sandia Report, SAND2000-1337, 2000.

15. B.J. Lutzenberger, D.L.Dickensheets; "Vertical Stiffening Members for Flatness Control of Surface Micromachined Structures;" Proc. SPIE, MOEMS and Miniaturized Systems, II, Vol. **4561**, pp. 238-246, 2001.

16. Y.N. Picard, D.P. Adams, O.B. Spahn, S.M. Yalisove, D. Dagel, J. Sobczak; "Low stress, low reflectivity thin films for MEMS mirrors;" *MRS Symposium*, U3.11, Vol. **729**, San Francisco, 2002.

17. B. D. Jensen, M.P. de Boer, N.D. Masters, F. Bitsie, D.A. LaVan; "Interferometry of Actuated Microcantilevers to Determine Material Properties and Test Structure Nonidealities in MEMS;" *IEEE Journal of Microelectromechanical Systems*, Vol. **10**, No. 3, pp. 336-346, September 2001.

18. N.D. Masters, M.P. de Boer, B.D. Jensen, M.S. Baker, D. Koester; "Side-by-Side Comparison of Passive MEMS Residual Strain Test Structures under Residual Compression;" *Mechanical Properties of Structural Films*, STP 1413, S. B. Brown and C. L. Muhlstein, Eds., American Society for Testing and Materials, West Conshohocken, PA, 15 September 2001.

19. M. Bicker, U. von Hulsen, U. Laudahn, A. Pundt, U. Geyer; "Optical deflection setup for stress measurements in thin films;" *American Institute of Physics: Review of Scientific Instruments,* Vol. **69**, Nr. 2, February 1998.

20. K. O'Donnell, J. Kostetsky, R.S. Post; "Stress in NiV, Cr and TiW Thin Films used in UBM and Backside Metallization;" IMAPS Flipchips, 2002.

21. W. Fang, C.H. Lee, H.H. Hu; "On the Buckling Behavior of Micromachined Beams;" *Journal of Micromechanics and Microengineering.*

22. W.N. Sharpe, Jr., B. Yuan, R. Vaidyanathan; "New Test Structures and Techniques for Measurement of Mechanical Properties of MEMS Materials;" *Proceedings SPIE Symposium on Micromachining and Microfabrication*, Vol. **2880**, pp. 78-91, 1996.

23. B.S. Majumdar, W.D. Cowan, N.J. Pagano; "Residual Stresses in MEMS Structures;" *Material Research Society Symposium*, Proceedings Vol. **594**, pp. 231-236, 2000.

24. L. Starman, Jr., J. Busbee, J. Reber, J. Lott, W. Cowan, N. Vandelli; "Stress Measurement in MEMS Devices;" *Modeling and Simulation of Microsystems*, ISBN 0-9708275-0-4, 2001.

25. F. Sandoval-Ibarra, J. Esteve; "Measuring Stress in Thin Films;" *Journal of the Mexican Society of Society of Instrumentation*, Instrumentation and Development Vol. **5** Nr. 2, pp. 99-103, July 2001.

26. F. Sandoval-Ibarra, J. Esteve, E. Guteirrez-Dominguez; "Stress in Thin Films: Analysis of Si3N4/Al Microstructures for Sensor Applications;" *Journal of the Mexican Society of Society of Instrumentation*, Instrumentation and Development Vol. **4** Nr. 3, pp. 3-5, 2000.

27. Y.H. Min, Y.K. Kim; "Modeling, design, fabrication, and measurement of a single layer polysilicon micromirror with initial curvature compensation;" *Sensors and Actuators*, Vol. **78**, pp. 8-17, 1999.

28. Reproducibility Data on SUMMiT V™ Short Course Slides, Chapter 19, 2000.

29. S. Chen, T. V. Baughn, Z. J. Yao, C.L. Goldsmith; "A New *In Situ* Residual Stress Measurement Method for a MEMS Thin Fixed-Fixed Beam Structure;" *Journal of Microelectromechanical Systems*, Vol. **11**, No. 4, pp309-316, August 2002.

30. M.S. Baker, M.P. de Boer, N.F. Smith, L.K. Warne, M.B. Sinclair; "Integrated measurement-modeling approaches for evaluating residual stress using micromachined fixed-fixed beams;" *Journal of Microelectromechanical Systems*, Vol. **11**, No. 6, December, 2002.

31. M.P. de Boer, N.F. Smith, N.D. Masters, M.B. Sinclair, E.J. Pryputniewicz; "Integrated Platform for Testing MEMS Mechanical Properties at the Wafer Scale by the IMaP Methodology;" *Mechanical Properties of Structural Films, STP 1413*, S. B. Brown and C. Muhlstein, Eds., American Society for Testing and Materials, West Conshohocken, PA, 2001.

32. J.A. Knapp, M.P. de Boer; "Mechanics of Microcantilever Beams Subject to Combined Electrostatic and Adhesive Forces;" *Journal of Microelectomechanical Systems*, Vol. **11**, No. 6, pp. 754-764, December, 2002.

33. M.S. Baker, M.P. de Boer, N.F. Smith, M.B. Sinclair; "Measurement of Residual Stress in MEMS to Sub Megapascal Accuracy;" *Society for Experimental Mechanics Annual Conference and Exposition*, Portland OR, June 4-6, 2001.

34. B.D. Jensen, F. Bitsie, M.P. de Boer; "Interferometric measurements for improved understanding of boundary effects in micromachined beams;" *Micromachining and Microfabrication,* Vol. **3875**, Santa Clara, CA, Sept. 20-22, 1999.

35. W.D. Cowan; "Materials impacts on Micro-Opto-Electro-Mechanical Systems;" *SPIE MOEMS and Miniaturized Systems*, M.E. Motamedi and R. Göring, Eds., Proceedings of SPIE Vol. **4178**, pp. 30-41, 2000.

36. D.C. Li, Z.Y. Xiao, W.G. Wu, Y. Yuan, S.J. Jin, Y.L Hao; "Simulation, Optimization and Measurement of MEMS Torsion Micro Mirrors for Optical Application;" *International Journal of Nonlinear Sciences and Numerical Simulation*, Vol. **3**, pp. 341-344, 2002.

37. Veeco WYKO Profiler Advanced User Training Course Slides, October 22-24, 2002.

38. http://hyperphysics.phy-astr.gsu.edu/hbase/phyopt/michel.html#c1

39. R. Sattler, P. Voight, H. Pradel, G. Wachutka; "Innovative design and modeling of a micromechanical relay with electrostatic actuation;" Journal of Micromechanics and Microengineering, Vol. 11, pp. 428-433, 2001.

40. J.V. Clark, D. Bindel, W. Kao, E. Zhu, A. Kuo, N. Zhou, J. Nie, J. Demmel, Z. Bai, S. Govindjee, K.S.J. Pister, M. Gu, A. Agogino; "Addressing the Needs of Complex MEMS Design"; MEMS 2002.

41. CoventorWare User's Manual, Coventor, Inc., Cary NC 27513, http://www.coventor.com.

42. J.M Gere, S.P. Timoshenko; *Mechanics of Materials 3rd SI Edition*; Chapman & Hall, London, 1991.

43. B. D. Jensen, M.P. de Boer, N.D. Masters, F. Bitsie, D.A. LaVan; "Interferometry of Actuated Microcantilevers to Determine Material Properties and Test Structure Nonidealities in MEMS;" *IEEE Journal of Microelectromechanical Systems*, Vol. **10**, No. 3, pp. 336-346, September 2001.

44. N.D. Masters, M.P. de Boer, B.D. Jensen, M.S. Baker, D. Koester; "Side-by-Side Comparison of Passive MEMS Residual Strain Test Structures under Residual Compression;" *Mechanical Properties of Structural Films*, STP 1413, S. B. Brown and C. L. Muhlstein, Eds., American Society for Testing and Materials, West Conshohocken, PA, 15 September 2001.

45. M. S. Baker, M.P. de Boer, N. F. Smith, L. K. Warne, M. B. Sinclair; "Integrated measurement-modeling approaches for evaluating residual stress using micromachined fixed-fixed beams;" *Journal of Microelectromechanical Systems*, Vol. **11**, No. 6, December, 2002.

46. M.P. de Boer, N.F. Smith, N.D. Masters, M.B. Sinclair, E.J. Pryputniewicz; "Integrated Platform for Testing MEMS Mechanical Properties at the Wafer Scale by the IMaP Methodology;" *Mechanical Properties of Structural Films, STP 1413*, S. B. Brown and C. Muhlstein, Eds., American Society for Testing and Materials, West Conshohocken, PA, 2001.

47. J.A. Knapp, M.P. de Boer; "Mechanics of Microcantilever Beams Subject to Combined Electrostatic and Adhesive Forces;" *Journal of Microelectomechanical Systems*, Vol. **11**, No. 6, pp. 754-764, December, 2002.

48. M.S. Baker, M.P. de Boer, N.F. Smith, M.B. Sinclair; "Measurement of Residual Stress in MEMS to Sub Mega Pascal Accuracy;" *Society for Experimental Mechanics Annual Conference and Exposition*, Portland OR, June 4-6, 2001.

49. B. D. Jensen, F. Bitsie, M.P. de Boer; "Interferometric measurements for improved understanding of boundary effects in micromachined beams;" *Micromachining and Microfabrication,* Vol. **3875**, Santa Clara, CA, Sept. 20-22, 1999.

50. http://www.efunda.com/home.cfm

51. S. Timoshenko, S. Woinosky-Krieger; *Theory of Plates and Shells 2nd Edition*; McGraw Hill International Editions, 1959.

52. G. Wang, B.V. Sankar, L.N. Cattafest, M. Sheplak; "Analysis of a Composite Piezoelectric Circular Plate with Initial Stresses for MEMS;" *Proceedings of 2002 ASME International Mechanical Engineering Congress and Exposition*, New Orleans, LA, November 17-22, 34337, 2002.

53. J. Sladek, V. Sladek; "A meshless method for large deflection of plates;" *Computational Mechanics*, Vol. **30**, pp. 155-163, 2003.

54. M.J. Madou; *Fundamentals of Microfabrication: The Science of Miniaturization, 2nd Edition*; CRC Press LLC, 2002.

55. P. M. Osterberg, R. K. Gupta, J. R. Gilbert, and S. D. Senturia, "Qualitative models for measurement of residual stress, Poisson ratio, and Young's modulus using electrostatic pull-in of beams and diaphragms", in *Technical Digest, Solid State Sensor and Actuator Workshop*, Hilton Head, SC, pp. 184-188, 1994.

56. http://www.supertex.com/

# APPENDICES

## Appendix A: Stress Gradient from Cantilever Beams

In order to analyze cantilever beams, the stress states before release, directly after release and after the beam bends must be taken into consideration. Prior to release, assume that the beam material has an average compressive stress $\sigma_0$ and also a stress gradient that results from the deposition. Once the parts are released, the beam length increases slightly to relieve the compressive stress so that the average stress goes to zero, however, the stress gradient remains. The stress gradient creates a moment in the beam and causes it to bend, which produces a curvature as shown in following figure.

**Curved Cantilever Beam on Left is More Compressive on Top; on Right, Beam is More Tensile on Top.**

The stresses involved in the cantilever can be expressed as follows

$$\sigma = \sigma_0 - \frac{\sigma_1}{(t/2)} z \qquad \text{(A.1)}$$

where $\sigma$ is the total axial stress in the beam, $\sigma_1$ is the stress after release, t the thickness of the beam and z is the downward direction. The moment created through the thickness of the beam is defined as

$$M_x = \int_{-t/2}^{t/2} Wz\sigma dz = -\frac{Wt^2\sigma_1}{6} \qquad \text{(A.2)}$$

where W is the width of the beam and $\sigma$ is again the total axial stress in the beam.

After release, the beam bends to a radius of curvature $\rho_x$ given by

$$\rho_x = -\frac{EWt^3}{12M_x} = \frac{Et}{2\sigma_1} \qquad \text{(A.3)}$$

where E is Young's modulus.

In addition to the x-direction moment, there is a transverse moment across the beam, which implies this is a biaxial stress gradient and Poisson effects must be included. Thus, for a beam the biaxial modulus is $\hat{E} = E/(1-\nu)$; where $\nu$ is Poisson's ratio. With some rearranging, the stress gradient becomes

$$\frac{\sigma_1}{t} = \frac{1}{2}\left(\frac{E}{1-\nu}\right)\frac{1}{\rho_x} \qquad \text{(A.4)}$$

## Appendix B: Residual Stress from Fixed-Fixed Beams

Beams supported at both ends with axial constraints have net residual stresses. Due in part to thermal effects, external axial loads or other residual stress effects, these stresses significantly affect the beam bending behavior. When these residual stresses cause the beam to buckle, or exert an out-of-plane deflection, residual stress can be calculated from the visual beam deflection.

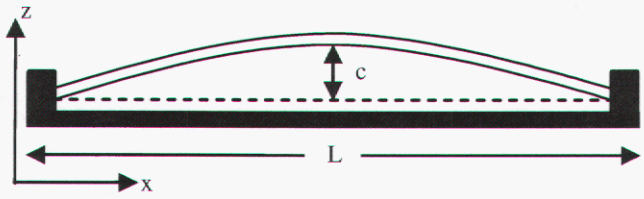


In order to derive the residual stress based on a buckled deflection, start with the post-buckled deflection curve of the smallest critical load. The beam is approximated by a cosine function as follows:

$$z(x) = \frac{c}{2}\left(1 + \cos\frac{2\pi x}{L}\right), \text{ -L/2} \le \text{x} \le \text{L/2} \qquad \text{(B.1)}$$

where c is the buckled amplitude and L is the length of the beam.

The arc length of the buckled beam is found by the integral in equation B.2 with a small angle approximation ($\sin(\theta) \approx \theta$):

$$l_{buckledBeam} = \int_{-L/2}^{L/2}\left[1 + \left(\frac{dz}{dx}\right)^2\right]^{1/2} dx \approx L\left[1 + \left(\frac{c\pi}{2L}\right)^2\right] \qquad \text{(B.2)}$$

The length of the post-buckled beam may also be expressed in terms of the average residual strain released by buckling, $\delta\varepsilon$.

$$l_{buckledBeam} = L(1 + \delta\varepsilon) = L\{1 + (\varepsilon_R - \varepsilon_{cr})\} \qquad \text{(B.3)}$$

where $\varepsilon_R$ is the residual strain in the material and $\varepsilon_{cr}$ is the critical buckling strain as given below.

A beam buckles due to a critical loading, where the critical elastic buckling strain $\varepsilon_{cr}$ is expressed in terms of the Euler buckling-load formula for fixed-fixed ends as follows:

$$\varepsilon_{cr} = \frac{4\pi^2 I}{L^2 A} = \frac{4\pi^2\left(\frac{bt^3}{12}\right)}{L^2(bt)} = \frac{\pi^2 t^2}{3L^2} \qquad \text{(B.4)}$$

where I is the moment of inertia of the beam, t is the beam thickness, and L is the beam length.

By substituting equations B.2 into B.3 and B.4 into B.3, the total residual strain becomes:

$$\varepsilon_R = \frac{\pi^2 t^2}{3L^2} + \frac{\pi^2 c^2}{4L^2} \qquad \text{(B.5)}$$

Residual stress can be found by applying Hooke's law to the total residual strain in the buckled beam. Hooke's law states: $\sigma = E\varepsilon$, where $\sigma$ is the material stress, E is the Young's

modulus, and ε is the material strain. The biaxial modulus $\hat{E} = E/(1-\nu)$ must also be used in this problem due to the axial and transverse loading. Thus, with a bit of rearranging, the residual stress becomes

$$\sigma_{res} = \frac{E\pi^2}{L^2(1-\nu)}\left(\frac{t^2}{3}+\frac{c^2}{4}\right) \qquad \text{(B.6)}$$

**Distribution:**

| Name | MS | Organization |
|---|---|---|
| Olga Blum Spahn | 0603 | 1742 |
| William Cowan | 0603 | 1742 |
| Daryl Dagel | 1080 | 1769 |
| Grant Grossetete | 0603 | 1742 |
| Bill Sweatt | 0603 | 1743 |
| Alex Grine | 0603 | 1743 |
| Sita Mani | 1080 | 1749 |
| Paul Resnick | 1080 | 1749 |
| David Adams | 0603 | 1743 |
| Fawn Gass | 1183 | 15425 |
| Michael Shaw | 1080 | 1749 |
| Dave Wick | 1188 | 15241 |
| Andy Boye | 0972 | 5710 |
| Jeff W. Martin | 0968 | 5714 |
| Mark V. Smith | 0978 | 5936 |
| Charles Sullivan | 0603 | 1742 |
| Dave Sandison | 1080 | 1769 |
| Harold Stewart | 1080 | 1749 |
| Jim Hudgens | 1080 | 1743 |
| Jay Jakubczak | 1071 | 1703 |
| Jeff B. Martin | 1219 | 5923 |
| Tech Library | 0899 | 9616 |
| Central Technical Files | 9018 | 8945-1 |
| Donna Chavez | 0123 | 1011 |